Economic Geology, v. 110, pp. 505–530

A Hydrothermal Ni-As-PGE Geochemical Halo Around the Miitel Komatiite-Hosted Nickel Sulfide Deposit, Yilgarn Craton, Western Australia*

Margaux Le Vaillant,[1,†] Stephen J. Barnes,[2] Marco L. Fiorentini,[1] John Miller,[1] T. Campbell McCuaig,[1] Peter Mucilli[3]

[1] *Centre for Exploration Targeting, School of Earth and Environment, Australian Research Council Centre of Excellence for Core to Crust Fluid Systems, The University of Western Australia, Perth, Western Australia 6009, Australia*

[2] *CSIRO/Earth Science and Resource Engineering, Kensington, Perth, Western Australia 6151, Australia*

[3] *Mincor Resources NL, Perth, Western Australia 6000, Australia*

Abstract

The remobilization of metals during postdeposition hydrothermal alteration of magmatic sulfide ores has the potential to result in large haloes, the recognition of which could potentially enlarge the detectable footprint of this ore type. The Miitel komatiite-hosted nickel sulfide deposit in Western Australia was used as a case study to investigate the nature and 3-D geometry of the geochemical halo created by the remobilization of base metals, gold, and platinum group elements (PGE) into the rocks surrounding the mineralization. At Miitel, anomalous metal enrichment is found in the country rocks surrounding the massive sulfides, up to 250 m away from the ore. This enrichment, detected using portable X-ray fluorescence (pXRF) and backed up by laboratory analyses, occurs in the Mount Edwards footwall basalt within decimeters of the contact with the overlying Widgiemooltha komatiites. It is associated with the presence of nickel arsenides. Gersdorffite and minor nickeline are concentrated within small quartz and carbonate veinlets, and are interpreted to form during the circulation of arsenic-rich hydrothermal fluids. Results of lead fire assay analyses and in situ laser ablation-inductively coupled plasma-mass spectrometer (LA-ICP-MS) analyses indicate high PGE concentrations (Pd and Pt) and minor gold associated with the observed nickel and arsenic enrichment. Results from a larger, regional-scale study, combined with this PGE enrichment, suggest that the massive nickel sulfides from the Miitel ore are the source of the remobilized nickel in the country rocks. The presence of Pd- and Pt-enriched trace arsenide phases in country rocks and shear zones may be a generally applicable proximity indicator for nickel sulfides in hydrothermally altered terranes.

Introduction

Magmatic nickel sulfide deposits are extremely challenging exploration targets. The prediction of their location area is generally reliable, but detecting their exact position is the real challenge. With deposits often composed of deep-seated, small, and narrow orebodies, many exploration targets can be blind. Moreover, many deposits have been structurally modified, such as Harmony (Duuring et al., 2007), and their ore shoots have been displaced from their original predictable position within magmatic channels. By taking a new approach and studying hydrothermal haloes, this project aims at enlarging the detectable footprint of magmatic nickel sulfide orebodies.

Exploration techniques for komatiite-hosted nickel sulfide deposits can be divided into two broad categories: predictive and detection techniques. Predictive techniques are generally useful at the craton to terrane scale (McCuaig et al., 2010) and include the identification of craton boundaries (Begg et al., 2010) and areas of enhanced magmatic flux (Barnes and Fiorentini, 2012; Fiorentini et al., 2012). Detection techniques are more useful at the deposit scale and mainly include geochemical and geophysical methods. Geochemical detection techniques include (1) search for evidence of crustal contamination (Lesher et al., 2001; Barnes et al., 2004; Fiorentini et al., 2012), (2) identification of channelized volcanic environments (Lesher, 1989; Hill, 1995; Barnes, 2006b), (3) thickness and nickel content of sediment units at basal komatiite contact (Bavinton, 1981), (4) detection of ruthenium depletion in chromite grains (Locmelis et al., 2013), and (5) detection of anomalous whole-rock enrichment and/or depletion of chalcophile element concentrations in komatiite units (Heggie et al., 2012; Barnes et al., 2013).

Few detection techniques have proved to be universally effective. Subtle platinum group element (PGE) enrichments in host komatiite units have been shown to extend up to 400 m away from the mineralization (Heggie et al., 2012; Barnes et al., 2013); however, this technique requires expensive high-precision analyses and fails where orebodies have been tectonically mobilized away from their original host rocks. A similar limitation applies to the use of Ni/Cr ratios, which can delineate ore-related channels (Barnes and Brand, 1999), but are not significantly more effective than nickel anomalies alone (Barnes et al., 2013). Geophysical methods mainly include electromagnetic techniques. The distance of detection (d) for downhole electromagnetism (DHEM), which is the standard technique, mainly depends on the shape and the size of the target, and varies between 0.5 to 1.5 times the smaller dimension of the orebody (pers. commun.: Bill Amann, Newexco Services Pty Ltd, 2003; Lisa Vella, Southern Geoscience Consultants, 2013; Jon Hronsky, Western Mining Services, 2013, 2014). In the case of the Miitel deposit, the orebodies are generally detectable 50 m away from the drill hole. The

† Corresponding author: e-mail, margaux.levaillant@research.uwa.edu.au

*A supplement for Digital Tables 1–5 is available at http://economicgeology.org/ and at http://econgeol.geoscienceworld.org/.

0361-0128/15/4294/505-22

Submitted: January 14, 2014
Accepted: May 20, 2014

main drawback of DHEM is the high false positive rate due to electromagnetic anomalies associated with sulfidic or graphitic metasediments, which makes it difficult to discriminate nickel-rich from barren sulfide bodies (Peters, 2006). This is a problem in many komatiite settings where sedimentary and exhalative sulfide units are present in close spatial association with the orebodies. In conclusion, magmatic nickel sulfide orebodies remain very difficult exploration targets, and to this date no completely effective tool (geochemical or geophysical) allows their detection.

Previous studies looking at hydrothermal halos around magmatic nickel sulfide deposits are few but show promising results. At the Barnet property, part of the Sudbury Cu-Ni-PGE camp in Canada, wide-scale mobility of nickel in hydrothermal solution in the footwall of the deposit has been highlighted by the presence of elevated concentrations of nickel in secondary amphiboles (Hanley and Bray, 2009). This work suggests that the transport of nickel could be associated with sodium- and halogen-rich fluids at 390° to 550°C, which interacted with country rocks during growth of amphiboles within 100 m of footwall sulfide veins. Another study by Layton-Matthews et al. (2007) at the Ni-Cu-PGE deposits of the Thompson nickel belt highlights enrichment in nickel, gold, palladium, and copper within sedimentary sulfide units adjacent to the Ni-Cu-PGE deposits. This enrichment is interpreted as being created during the mobilization of fluids generated by the metamorphism of both the ore zones and their host rocks (Bleeker, 1990; Burnham et al., 2003). Moreover, there are an increasing number of studies on hydrothermal nickel accumulations, indicating large amounts of remobilization of nickel from massive sulfide sources, possibly on a scale of hundreds of meters (González-Álvarez et al., 2013a, b; Keays and Jowitt, 2013; Pirajno and González-Álvarez, 2013). All these results show that, contrary to the common belief of nickel being an extremely immobile element, specific fluids in particular environments may have the capacity to remobilize nickel from a massive sulfide source. Unfortunately, information on the aqueous speciation and hydrodynamic properties of nickel species likely to be important in natural systems is extremely limited (Liu et al., 2012). Therefore, very few studies have tried to understand the behavior of nickel and quantitatively model its transport in hydrothermal fluids for expected ligands such as chloride (Seward and Barnes, 1997) and at appropriate temperatures (400°–800°C; Lin and Popp, 1984; Fahlquist and Popp, 1989).

In this contribution, the results of a case study on the Miitel komatiite-hosted nickel sulfide deposit in Western Australia are presented utilizing a new approach and studying hydrothermal haloes near the deposit. This project aims at enlarging the detectable footprint of magmatic nickel sulfide orebodies by identifying, in immediately adjacent country rocks, a geochemical halo produced by the circulation of postmagmatic hydrothermal fluids within mineralized ultramafic systems and their immediate country rocks. This halo would be created by secondary processes, and the "stain" created would not depend on the original setting of the ore. Provided that this geochemical anomaly is spatially constrained and potentially zoned, this halo could be used for orebody detection in association with the traditional methods listed above.

Geologic Setting

Regional geology

The Miitel deposit is an Archean komatiite-hosted nickel sulfide deposit located within the Eastern Goldfields Superterrane of the Yilgarn craton in Western Australia (Fig. 1). The deposit is located on the eastern flank of the Widgiemooltha dome (Seat et al., 2004; Fig. 1), within the fault-bounded Coolgardie domain of the Kalgoorlie terrane (Swager, 1997).

The Widgiemooltha dome sequence is mainly composed of ultramafic, mafic, and felsic metavolcanic rocks, metasediments, and minor mafic and felsic intrusive rocks (Hayward, 1988). The stratigraphic sequence around the Widgiemooltha dome can be divided in two portions. The lower portion contains two cycles of komatiitic lavas (the Mount Morgan and the Widgiemooltha komatiites) contained within tholeiitic extrusive and intrusive rocks. The komatiite lavas contain minor graphitic to cherty interflow horizons and minor high Mg mafic flows (Fig. 1). These cycles are considered to be thrust repeats of the same stratigraphic units (Archibald et al., 1978; Fig. 2). The upper portion of the stratigraphy is composed of felsic volcaniclastic rocks, associated sediments, and a mixed clastic assemblage (Spargoville felsic rocks). Granitoids, rhyolitic porphyry dikes, pegmatites, and Proterozoic dolerite dikes crosscut the sequence (McQueen, 1981; Hayward, 1988; Fig. 1). The Miitel deposit massive sulfide bodies are found at the contact between the Mount Edwards tholeiitic basalt and the overlying Widgiemooltha komatiites in the upper cycle.

The peak metamorphic conditions of the Widgiemooltha dome region are estimated by Archibald et al. (1978) to be at mid-amphibolite facies, with temperatures around 550° to 620°C and pressures of 3.2 to 4 kb. The peak metamorphic temperature is found to increase from northeast to southwest across the dome. The Widgiemooltha komatiites on the east flank of the dome, including those hosting the Miitel ore, are pervasively metamorphosed to talc-carbonate assemblages (Hayward, 1988), which are only stable to lowermost amphibolite facies (Barnes and Hill, 2000). These talc-carbonate assemblages imply either retrograde carbonate metasomatism of originally higher-grade rocks, or that the metamorphic grade is not as high at Miitel as previously assumed for this portion of the terrane.

Many studies describe the structural history of the East Yilgarn craton; the work by Swager (1997) summarizes 10 years of prior research by many different authors (Archibald et al., 1978; Platt et al., 1978; Hammond and Nisbet, 1992; Williams and Whitaker, 1993), and a subsequent summary by Blewett et al. (2010) presents a structural-event framework incorporating a subsequent decade of research. Blewett et al. (2010) describe six phases of deformation: (D_1) ENE-WSW extension, (D_2) ENE-WSW compression, (D_3) extension, (D_4) (a and b) compression and strike-slip movement, (D_5) NE-SW contraction and dextral strike-slip, and (D_6) low-strain vertical shortening. The D_4b episode is interpreted as being the event during which most of the region's gold was deposited.

Geology of the Miitel deposit

The Miitel deposit is a "type 1" komatiite-hosted nickel sulfide deposit (Lesher and Keays, 2002) with close similarities

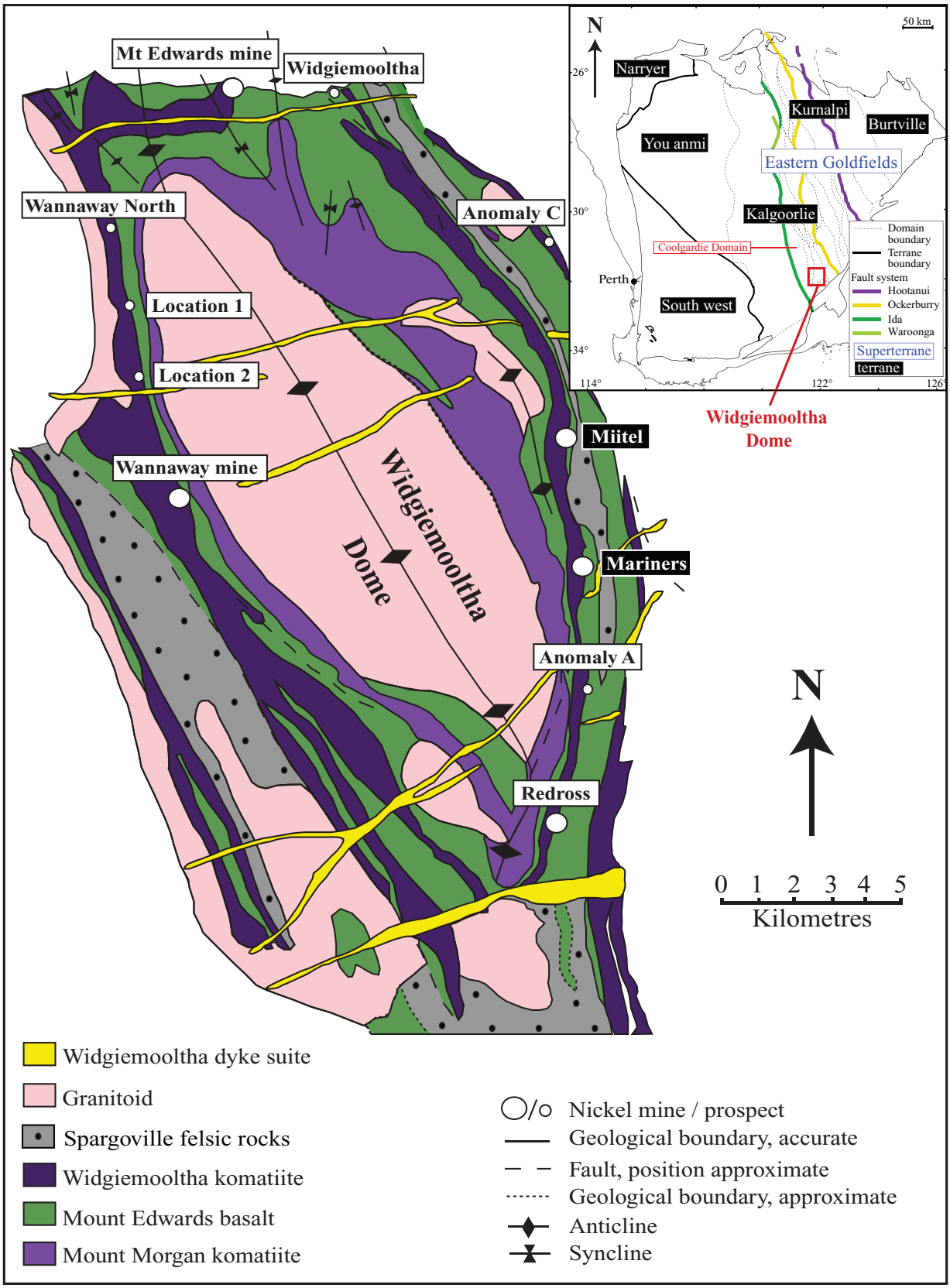

FIG. 1. Geologic map of the Widgiemooltha dome area locating existing nickel sulfide mines and prospects (adapted and modified after Seat et al. (2004) and McQueen (1981), originally modified after Willet et al. (1978)). Inset simplified geologic map of the Yilgarn craton showing the location of the Widgiemooltha dome, modified from Cassidy et al. (2006).

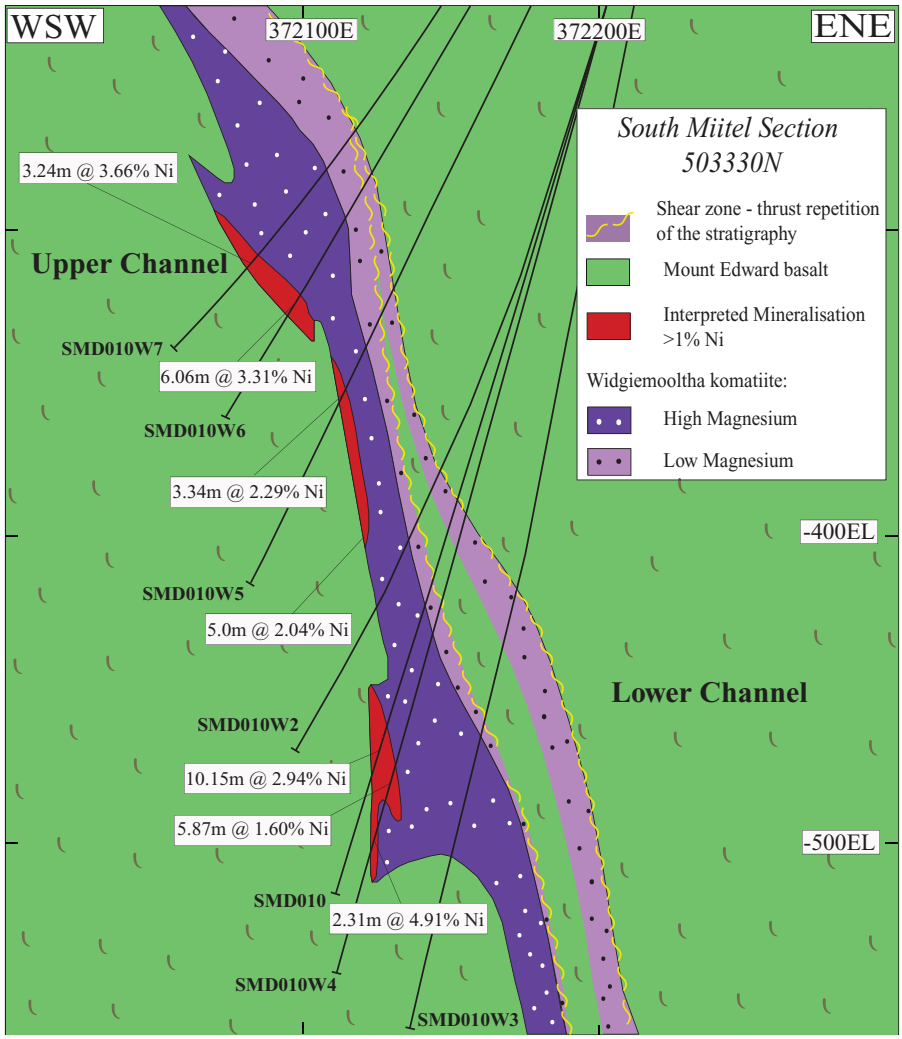

FIG. 2. Geologic cross section (WSW-ENE) through the Miitel mineralized system. The location of the cross section is indicated on the 3-D model in Figure 3.

to the well-documented deposits of the Kambalda dome (Gresham and Loftus Hill, 1981). It is located in the lower portion of the Widgiemooltha dome stratigraphy. The ore is hosted by the Widgiemooltha komatiites, resting either directly on the Mount Edwards basalt or on a thin veneer of sulfidic sediments that was deposited during a hiatus between tholeiitic volcanism and the emplacement of komatiite flows (Marston, 1984). To the end of June 2013, Miitel has produced 2.13 million tons (Mt) of ore at an average grade of 2.98% nickel, for 63,600 t of contained nickel (Mincor internal operational report, unpub.). With past production added to June 2013 ore reserves, Miitel's total known nickel endowment is in excess of 73,400 t of nickel metal (Mincor internal operational report, unpub.). Exploration and production are still active and Miitel may turn out to be one of the larger orebodies of the of Kambalda region.

The Miitel deposit is composed of numerous shallow (15°–30°), southerly plunging massive nickel sulfide ore pods, occupying a boomerang-shaped channel that has been defined over a length of more than 5 km at the embayed contact between the Mount Edwards basalt and the Widgiemooltha komatiites (Fig. 3). The strike of the ore-bearing contact is approximately 345°, and dips are steeply eastward (75°–85°; Cairns et al., 2003). The average dimensions of the ore pods are 50 to 75 m of original horizontal width and 30 to 250 m on the long axis. Ore pods are commonly flanked on one or both sides by "pinchouts," areas where the nickel sulfides are in contact with basalt on both sides (Fig. 2). These are interpreted as the result of small-scale thrusting of the footwall basalt over the edges of the massive sulfide bodies (Stone and Archibald, 2004). The ore pods are composed of massive ore (>80% sulfides), generally 1 to 2 m thick, overlain in turn by matrix or net-textured ores (40–80% sulfides, 2–5 m thick) and disseminated (2–5% sulfides) nickel sulfides. Only massive sulfides are present in pinchout positions.

The Mount Edwards basalt is composed of a tremolite-actinolite assemblage. It has also been subjected to a pervasive potassium overprint producing accumulations of biotite in a weak to moderate foliation. The Widgiemooltha komatiite is composed of coarse-grained subhedral magnesite porphyroblasts uniformly distributed throughout an extremely fine-grained talcose matrix with minor chlorite (Cairns et al., 2003). The original lithology is interpreted as an olivine

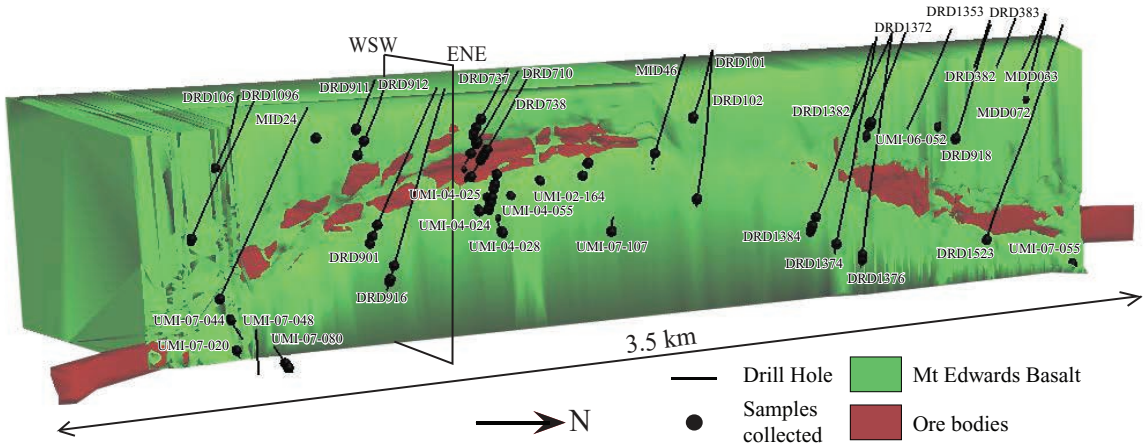

FIG. 3. View of the 3-D model of the Miitel Deposit in gOcad®. Only the Mount Edwards basalt (in green) and the orebodies (in red, nickel resources defined by a 1% nickel cut off) are represented for clarity. The section (ENE-WSW) on the model is shown in Figure 2.

mesocumulate forming the lower B zone of a channelized komatiite flow (Lesher et al., 1984). The Miitel ore is composed of pyrrhotite ($Fe_{1-x}S$) as the main sulfide phase and pentlandite ($(Ni,Co)_9Fe_{11}S$ as the dominant nickel-hosting phase with subordinate chalcopyrite ($CuFeS_2$), magnetite (Fe_3O_4) and minor pyrite (FeS_2). The ore has been modified by various phases of deformation and contains mineralogical layering defined by variable proportions of pentlandite. Arsenic has also been added to the system by hydrothermal fluids localized along specific structures, and gersdorffite (NiAsS) and rare nickeline (NiAs) are present in trace amounts in areas of the orebody. Arsenic grades, for routine grade control sampling, range from 10 to 50,000 ppm, with grades above 5,000 ppm restricted to arsenic contaminated ore zones. The average arsenic value for the total known Miitel orebody is 468 ppm.

This study uses the structural framework of Cairns et al. (2003), locally recognizing five deformation stages. D_1 and D_2 represent a progressive transition from large-scale thrusting to folding with increasing compression (both correspond to D_1 and D_2 from Blewett et al. (2010)). D_3 to D_5 are interpreted as being closely related in time. D_3 resulted in east-dipping (80°–90°) northwest faults (330°–345°) creating dextral dislocation and separating the ore into multiple pods. D_4 produced shallow WSW-dipping ductile shearing with a reverse dextral movement (max. extent of ~5 m). Anomalously high arsenic concentrations are observed where these D_4 structures crosscut the ore; introduction of arsenic is therefore thought to be epigenetic, overprinting the nickel sulfide ore, and associated with at least some of the talc carbonate alteration in the ultramafic rocks. The orogenic gold event which produced many economic deposits in the Kambalda-St. Ives area is thought to be coeval with the circulation of these arsenic rich fluids. D_3 and D_4 correspond to D_4 (a and b) from Blewett et al. (2010). Finally, subvertical EW-striking basaltic joints are attributed to the brittle D_5 event.

Materials and Methods

In order to establish the presence and the nature of any possible geochemical haloes around the Miitel deposit, sampling was focused along possible fluid pathways intersecting massive sulfides. First, samples collected were analyzed by portable X-ray fluorescence (pXRF) in order to highlight anomalous concentrations, without destroying the samples. Any anomalous results were then followed up by a petrographic study of the analyzed area, as well as detailed laboratory analyses. The nickel-bearing mineral phases associated with anomalous results were analyzed in situ by electron microprobe and by laser ablation-inductively coupled plasma-mass spectrometry (LA-ICP-MS). Finally, all the geochemical results were combined with structural information to create a 3-D model of the Miitel deposit.

Sampling

Two sets of samples were collected for this study. Samples from the first set (batch 1) come from the vicinity of the Miitel deposit. Sampling focused on the contact between the Widgiemooltha komatiites and the underlying Mount Edwards basalt, on the premise that this contact acted as a pathway for hydrothermal fluids. A total of 157 samples were collected, most of them in close proximity to the footwall contact (0–30 m), except for a few background samples collected up to 100 m away from the contact. The samples were located at various distances from the orebodies, 5 to 300 m away, vertically below and above the main mineralized channel (Fig. 3). Primary magmatic sulfide veins have been reported in footwall basalt in this style of deposit (Lesher and Groves, 1986) but none were observed at Miitel. For the purposes of this study, the basalt samples were selected to be free of any visible sulfide component.

The second set of samples (batch 2) was collected along a regional section between the Miitel and the Mariners deposits (3–4 km south of Miitel, Fig. 1). Seven drill holes were chosen along this section, each separated by approximately 500 m (Fig. 4A) and 53 samples were collected. As with the first batch, sampling focused on the contact between the Widgiemooltha komatiites and the underlying Mount Edwards basalt.

Portable XRF analyses

First, 84 of the samples from batch 1, collected around the Miitel deposit, and all the sample from batch 2, collected

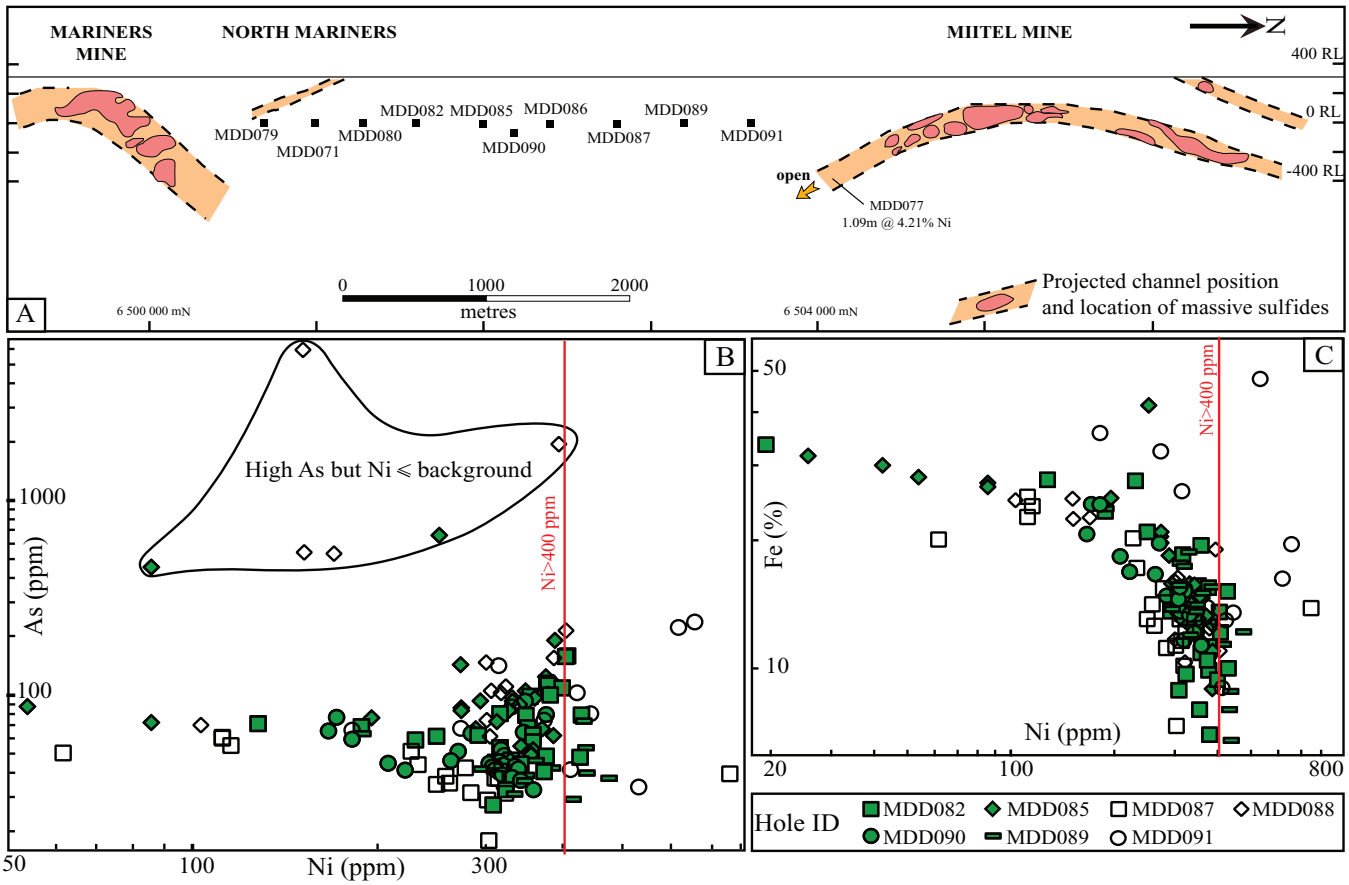

FIG. 4. Location and results of the regional study. (A) Long section between the Miitel and the Mariners deposits showing the location of the sampled drill holes. (B) Results obtained with portable XRF analyses collected on samples taken at the contact between the Mount Edwards basalt and the Widgiemooltha komatiites in seven chosen drill holes spread along this regional section. The drill holes analyzed are represented on the section (A).

along the regional transverse between the Miitel and the Mariners deposits, were analyzed for a range of major and trace elements (Si, Ca, K, Ti, Cr, Ni, Zn, Cu, Zr, Sr) using an Olympus-InnovX-X500 desktop X-ray fluorescence analyzer (pXRF), which has a 10 W, 50kV tantalum X-ray tube with a high-precision, large area silicon drift detector. Between 5 and 15 analyses were collected per sample on coarsely polished drill core surfaces over 10 to 60 cm long, following the analytical protocol described by Le Vaillant et al. (2014). Calibration of the instrument was completed using 28 matrix-matched internal reference materials of similar composition to the analyzed samples. These reference materials were selected among samples collected at the Miitel deposit and previously analyzed by Ultra Trace laboratories in Perth, Western Australia, by laboratory X-ray fluorescence (lab XRF), ICP-MS, and inductively coupled plasma-atomic emission spectrometry (ICP-AES) methods. These materials scan most of the range of concentrations encountered in the dataset as a whole, for each element of interest. The calculated pXRF detection limits vary between 2 ppm for Zn and 0.15 wt % for S. Finally, instrumental and sample precision were determined, the instrumental precision (calculated as two times the relative standard deviation of repeated analyses) varies from 0.9% for Si to 7.4% for Zn, and the sample precision varies from 5% for Zr to 63% for S (calculated by repeated analyses of a representative fine-grained basalt from Miitel). All the results of detection limit calculations and precision calculations are described in Digital Table 1.

In order to evaluate the degree of agreement between lab XRF and pXRF, results from Ultra Trace laboratories were compared with the average of the results of multiple pXRF analyses collected on the same samples (between 5 and 10 analyses were collected per sample). 56 samples (komatiites, basalts, and a couple of sediments) already analyzed by pXRF were sent to the Ultra Trace laboratories in Perth for lab XRF analyses as well as ICP-MS and Lead fire assays. Figure 5 shows the results of this comparison study. Both pXRF and laboratory analyses concur on the background composition of the Mount Edwards basalt and the Widgiemooltha komatiites. These results allow us to validate any anomalous values that will be detected with pXRF, and to reject the possibility that they represent analytical artifacts.

Laboratory analyses

Of the samples collected across the contact between the basalt and the komatiite, and analyzed by pXRF, 26 were divided by lithology (23 basalt, 22 komatiites, 5 of mixed lithology at the contact, and 1 contact sediment). These samples were analyzed by Ultra Trace laboratories in Perth for major elements, trace elements, and PGE. The analytical protocol is

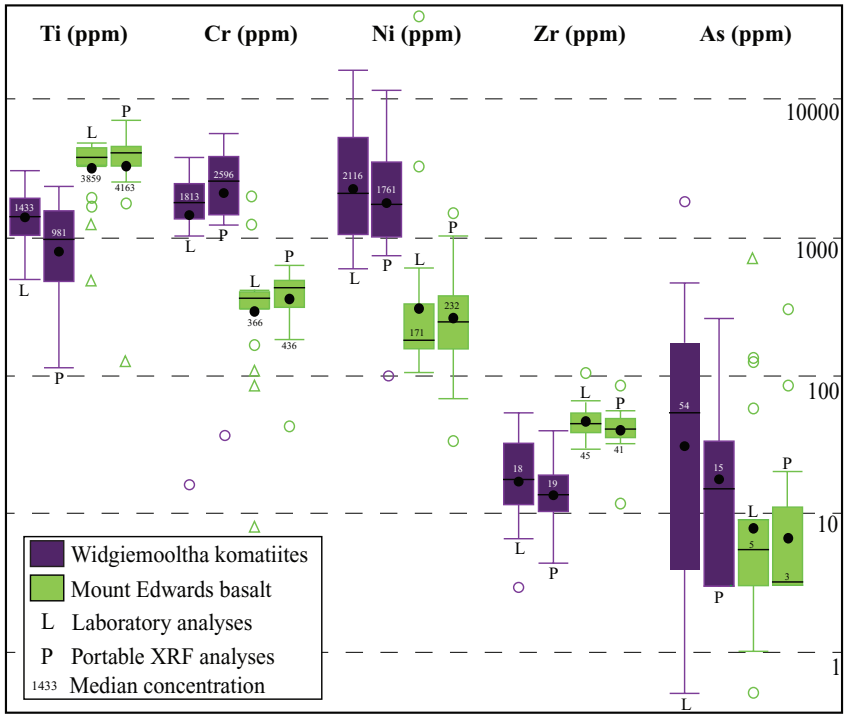

FIG. 5. Comparison of results obtained between laboratory XRF and portable XRF (pXRF) for komatiite and basalt samples. The central box is the middle 50% of the data from Q1 (bottom of the box which represents the 25th percentile) to Q3 (top of the box which represents the 75th percentile). An outlier (circle) is further than 1.5*(Q3-Q1) from the box. A far outlier (triangle) is farther than 3.0*(Q3-Q1) from the box. The whiskers are the extreme values that are not outliers. The line in the middle of the box represents the median and the black dot represents the mean.

as follows. Once dried and sorted, samples are crushed with a steel jaw crusher, and pulverized in a vibrating disc pulverizer with a steel bowl and puck. The main oxide concentrations are obtained by XRF spectroscopy on part of the samples previously cast using 12:22 flux to form a glass bead (SiO_2, Al_2O_3, CaO, Fe_2O_3, K_2O, MgO, Na_2O, P_2O_5, TiO_2, MnO, BaO, V_2O_5, Cr_2O_3, Cu, Ni, Zn). The same pulverized samples are also digested and refluxed with a mixture of acids (hydrofluoric, nitric, hydrochloric, and perchloric acids). This method approaches a total digest for most mineral phases; however, a few refractory minerals such as zircon and chromite are not completely attacked, although recoveries of better than 90% are indicated for most samples (unpub. CSIRO data). The obtained solutions are analyzed by both ICP-MS (La, Ce, Cs, Pr, Nd, Sm, Eu, Gd, Tb, Dy, Ho, Er, Tm, Yb, Lu, Ga, Y, Nb, Pb, Th, Hf, Rb, Sn, Sr, Ta, U, Zr) and ICP-optical emission spectrometry (ICP-OES; Fe, Co, Cr, K, Mn, P, Sc, Ti, V) to obtain trace element concentrations. Finally, a lead fire assay process gave a total separation of Au, Pt, and Pd, which are then determined by ICP-MS. For quality control purposes, pulps of 13 of the samples analyzed by lead fire assay at Ultra Trace laboratories were also sent to Geoscience Laboratories in Sudbury for nickel sulfide fire assay, with successful results (correlations between $(Pd,Pt)_{Ultra\ Trace}$ and $(Pd,Pt)_{Geolab}$ of 0.99). More details on the results of the comparison study are given in Digital Table 2.

Petrographic study

Portable XRF analyses highlighted the presence of anomalous nickel concentrations. Thin and thick sections (30 and 100 μm thick) were prepared focusing on the cm-scale areas where pXRF analyses reported high nickel concentrations. These samples were studied by optical and scanning electron microscope (SEM). The SEM used was a Phillips (FEI) XL40 controlled pressure SEM fitted with a Bruker EDS at CSIRO in Kensington, Western Australia. The SEM was operated at 30kV and a chamber vacuum of about 0.5 mb. Images were collected with a Robinson backscattered electron detector and spectra collected for mineral identification were processed using the Bruker standardless oxide method.

XRF microscopy

Four samples (DRD918-358.6, DRD912-239.5, SMD015-W7-674.5, and SMD015-W7-671.7), characteristic of the samples containing nickel anomalies, were chosen to investigate mineralogical associations in more details. Two of them (DRD918-358.6 and DRD912-239.5) were analyzed at the Australian synchrotron, and two were mapped using micro-XRF at the Australian Resources Research Centre (ARRC) in Perth (SMD015-W7-674.5 and 671.7). The Maia detector array on the XRF microscopy beamline, at the Australian Synchrotron in Melbourne, allows the production of elemental maps with approximately 10 ppm detection limits and a resolution of up to 2 μm (Ryan et al., 2010). Detailed maps were produced over areas of about 3 cm^2 using a beam energy of 18.5 keV, a spot size of 2 μm and dwell times per pixel of 0.97 ms giving an effective spatial resolution of 4 μm. These elemental maps represent an effective way of precisely mapping element association on the scale of a few cm^2 in a matter of a few hours. The micro-XRF maps produced at the

Australian Resources Research Centre were obtained using a Bruker M4 TORNADO™ equipped with a rhodium target X-ray tube operating at 50 kV and 500 nA and an XFlash® silicon drift X-ray detector. Analyses are then quantified using the Bruker ESPRIT software. Maps were created using a 25-μm spot size on a 25-μm raster with dwell times of 5 ms per pixel. Maps are represented as unquantified background-corrected peak height data for Kα peaks for each element.

LA-ICP-MS spectrometry

LA-ICP-MS at the University of Québec at Chicoutimi (UQAC) was used to measure concentrations of ^{34}S, ^{57}Fe, ^{59}Co, ^{61}Ni, ^{65}Cu, ^{66,68}Zn, ^{75}As, ^{82}Se, ^{95}Mo, ^{101}Ru, ^{103}Rh, ^{105,108}Pd, ^{109}Ag, ^{111}Cd, ^{118}Sn, ^{121}Sb, ^{128}Te, ^{185}Re, ^{189}Os, ^{193}Ir, ^{195}Pt, ^{197}Au, ^{208}Pb, and ^{209}Bi. Analyses were carried out on nickel arsenides contained in (1) small hydrothermal veins, in two of the Mount Edwards basalt samples mapped at the Australian Synchrotron (DRD918 and DRD912), and (2) within an arsenic enriched area of the ore (sample DRD738). The LA-ICP-MS instrument consists of an Agilent 7700x ICP-MS coupled with a Resonetics RESolution M50-E, 193 nm Excimer (5 ns pulse width) laser recently equipped with the S155 Dual Volume Sample Cell. Details of data reduction, interference corrections, calibration, and precision and accuracy tests are given in the Appendix following the Reference section.

3-D modeling

All the observations obtained with the various analytical techniques described above were combined with geological data and plotted spatially using Leapfrog® and gOcad® 3-D modeling software. Two models of the distribution of the arsenic in the Miitel komatiite system were produced in Leapfrog® using the Mine assay database composed of 51,880 analyses. The first model was done using an isotropic interpolation in order to observe arsenic variations without adding any interpretation bias, using the following parameters: a nugget effect of 0.5, a resolution of 5 m, an accuracy of 0.3, and a constant drift (ordinary kriging). The second model was produced using a spheroidal interpolation and incorporating a structural trend. The structural trend used to guide the interpolation of the arsenic concentration was produced in Leapfrog® using the orientation of the shallow-dipping S-SSW splay structures interpreted by Cairns et al. (2003) as structures carrying the arsenic-rich fluids. Parameters used for this second model were a nugget effect of 0.5, a range of 200 m, a resolution of 5 m, an accuracy of 0.3, and a constant drift (ordinary kriging).

Results

Miitel deposit scale pXRF analyses (batch 1)

The concentrations of As, Ca, Cr, Cu, Fe, K, Mn, Ni, S, Si, Sr, Ti, Zn, and Zr were determined by pXRF on lightly polished core surfaces for all the samples collected along the footwall contact. The lithology associated with each analysis was controlled using a Cr, Ti, Zr ternary diagram (Fig. 6A; Hallberg, 1984). This diagram allows the clear distinction between ultramafic rocks, basalts, and sediments. Apart from five analyses classified as basalt and plotting either in the komatiite or sediments field, there is a very good cluster of the data for the different rock types on the Cr, Ti, Zr ternary diagram. Misclassified samples probably represent mixed rock types.

The background nickel value measured for the Mount Edwards basalt, away from the footwall contact, is 127 ± 32 ppm (Median ± SD) for samples analyzed by laboratory XRF, and 249 ± 75 ppm for samples analyzed by pXRF (samples from batch 1 only). The difference in background values for nickel obtained with laboratory analyses and with pXRF is due to the nuggety behavior of nickel (Fig. 5; App. Table A1). Portable XRF analyses will only represent 1.5 cm^2 of rock, creating a more heterogeneous signature of the nickel composition of the rock, compared with 30-cm-long homogenized samples sent to the laboratory. In this study, within the pXRF results, nickel values were considered anomalous above 400 ppm (median + 2 · SD).

In order to visualize and interpret data obtained at the scale of the Miitel deposit, a Ni/Cr versus Ni/Ti diagram (Barnes et al., 2004) was used (Fig. 6B). This plot, originally intended to delineate volcanic facies in komatiites, is an effective way of separating the two different rock types observed, owing to the contrast in Ti and Cr contents between komatiites and basalts. The average ratios, using background samples, are: 0.07 ± 0.03 (Median ± SD) Ni/Ti and 0.5 ± 0.2 Ni/Cr for the Mount Edwards basalt compared with 0.29 ± 0.73 Ni/Ti and 0.41 ± 0.81 Ni/Cr for the Widgiemooltha komatiites.

The particular advantage of this plot in the present context is that addition or removal of nickel shows up clearly as linear trends of unit slope; hence, the plot serves to identify basalt samples that have been enriched in nickel. Among results of the pXRF analyses collected on basalt samples, over 62 analyses stand out from the Mount Edwards basalt background composition with anomalously high nickel contents above 400 ppm. The basalt samples analyzed in this study are consistently free of primary sulfides, so the linear trend observed (Fig. 6B) is not due to presence of a magmatic nickel sulfide component.

Figure 7 shows the relationship between nickel and the various other elements analyzed with pXRF for the basalt component of all the contact samples from the Miitel deposit (sample batch 1), (All results of pXRF analyzes tabulated in Digital Table 3). No visible correlations exist between Cr, Ti, Zr, and Ni (Fig. 7A-C). A correlation between nickel and arsenic is observed when arsenic is detectable in the sample (correlation coefficient R = 0.48; Fig. 7A); all the samples containing arsenic above 35 ppm also contain high concentrations of nickel (>400 ppm). A correlation between Ni and S can also be observed (R = 0.51; Fig. 7B), especially for nickel values above background (>400 ppm). Samples with elevated sulfur but background nickel represent samples containing "barren" sulfides, mainly pyrrhotite. Finally, in Figure 7C, nickel seems to be anticorrelated with iron when nickel values are close to background level (R = –0.69 for Ni <400 ppm), but positively correlated for nickel values above background (R = 0.37 for Ni >400 ppm).

Regional-scale pXRF analyses (batch 2)

Figure 4 presents the results of the pXRF analyses collected on contact samples from the regional study with seven drill holes spread along 3.5 km between the Miitel and the

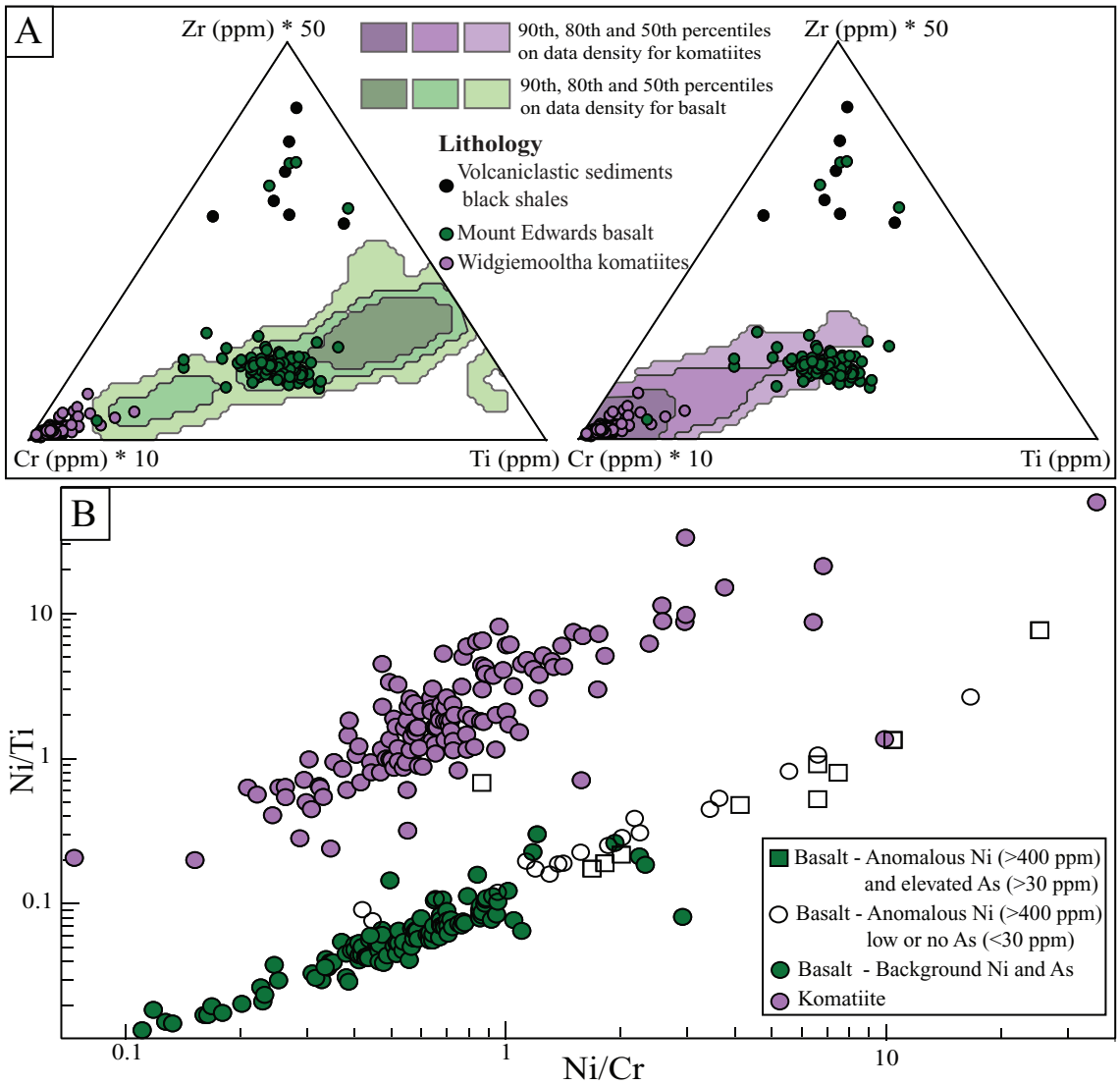

FIG. 6. Results of portable XRF (pXRF) analyses. (A) Ternary diagram used to validate the rock identification and separation in various lithologies. The density contours were produced on data density plots for komatiites from the database of Barnes and Fiorentini (2012) and on density plot for Lunnon-type low Th basalts from the database of Barnes et al. (2012). (B) Ni/Ti vs. Ni/Cr diagram, adapted from Barnes et al. (2004), where it was used as a tool for the assessment of komatiite prospectivity for nickel sulfides.

Mariners deposits (batch 2: see Digital Table 4 for full data). Only results of analyses collected on the basalt component of the contact sample are presented in Figure 4. On the Ni vs. As plot (Fig. 4B), a majority of the results cluster with nickel values around 320 ± 112 ppm (Median ± SD). Few samples seem to have been depleted in nickel, but only three analyses show elevated nickel. Within these three, two also contain elevated arsenic and are located in the drill holes closest to the Miitel ore (MDD091). Although very few samples show elevated nickel, many have elevated arsenic concentrations above 100 ppm, and apart from two, none of these samples have elevated concentrations of nickel. Finally, the same noncorrelation between iron and nickel that is evident in basalt samples from within the vicinity of the Miitel deposit (batch 1) with nickel at background levels (Ni <400 ppm) can be observed in Figure 4C (R = –0.54).

Mineralogy of the Mount Edwards basalt

Figure 8 illustrates the various textures and alteration patterns observed within the Mount Edwards basalt in samples located between 26 and 53 m away from the footwall contact and the ore. The regional low amphibolite facies metamorphism, associated with the circulation of CO_2-rich fluids, transformed the original basaltic assemblage into a tremolite-actinolite and carbonate (mainly ankerite) assemblage with relicts of plagioclase. Potassium-rich fluids, probably synpeak metamorphism, created zones enriched in biotite, commonly aligned in a weak to moderate foliation. The metamorphic amphiboles (tremolite and actinolite) are replaced by chlorite in places. Finally, in many samples a pervasive hydrothermal alteration silicified the basalt, creating a fine-grained quartz overprint.

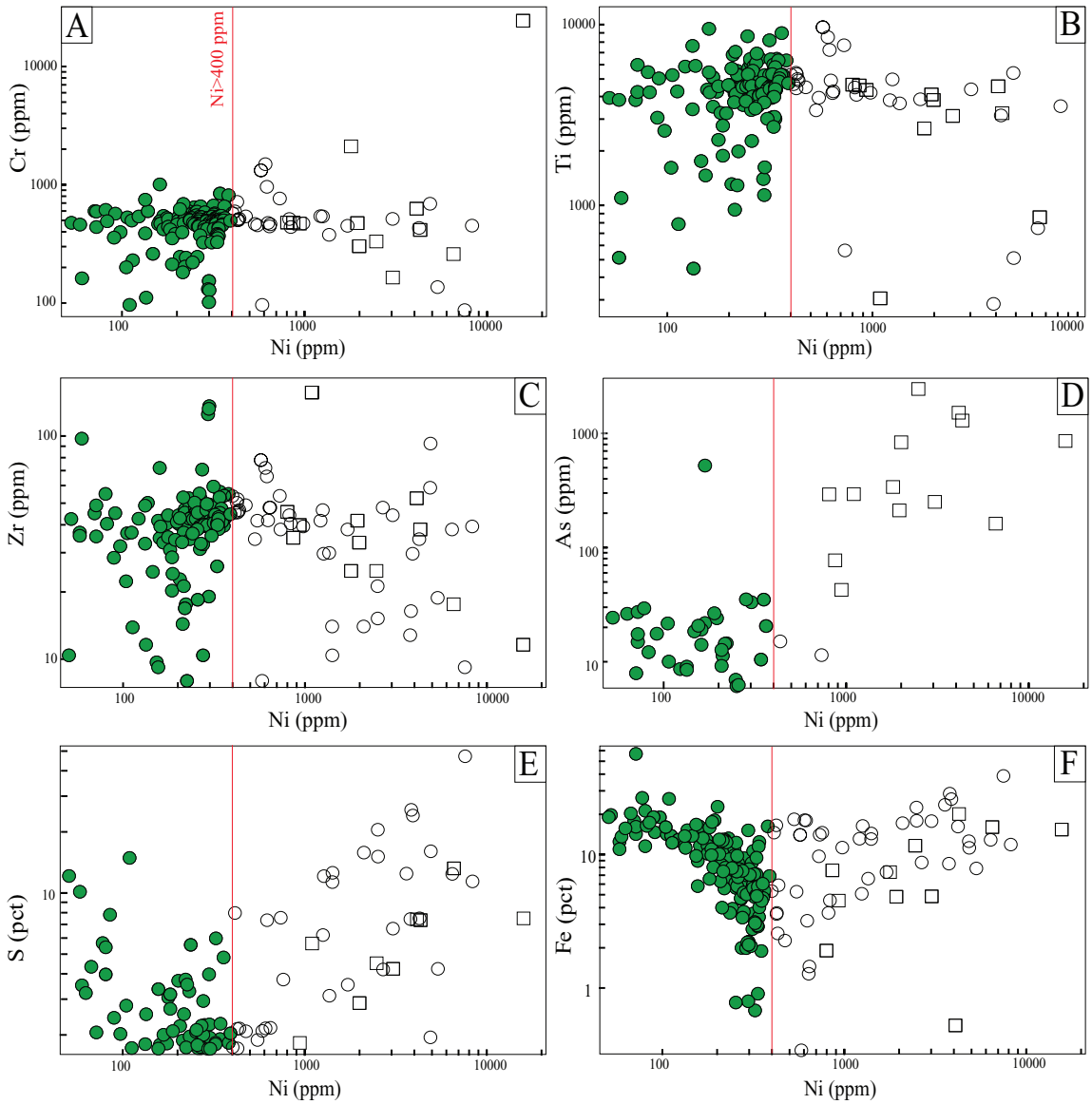

FIG. 7. Geochemical plots using the results of portable XRF analyses collected on samples taken at the contact between the Mount Edwards basalt and the Widgiemooltha komatiites all along the mineralized channel at Miitel (batch 1).

XRF microscopy

High resolution XRF microscopy element maps and micro XRF maps were produced for nickel-enriched areas of four basalt samples: DRD912-239.5, DRD918-358.6, SMD015-W7-674.5, and SMD015-W7-671.7 (Fig. 9). Figure 9 is composed of two XRFmaps (produced at the Australian Synchrotron) and two micro-XRF element maps (produced at ARRC), showing the distribution of nickel, iron, and arsenic within areas where anomalous nickel was detected by pXRF. These maps highlight a very clear association between the spatial distribution of nickel and arsenic within veins and vein selvedges. These small veins also contain lesser amounts of iron sulfides (pyrrhotite), localized areas enriched in copper sulfides (chalcopyrite) and, in the case of sample SMD015-W7-671.7, small amounts of pentlandite, mostly finely intergrown with pyrrhotite.

Mineralogy and chemistry of the samples containing anomalous nickel concentrations

Petrographic studies of the Mount Edwards basalt samples containing anomalous nickel, confirmed by mineral identification using SEM–energy-dispersive X-ray spectroscopy (EDS), show that nickel is mostly present as gersdorffite (NiAsS), minor nickeline (NiAs), occasionally as pentlandite ($(Ni,Fe)_8S_9$) exsolutions in pyrrhotite ($Fe_{1-x}S$), and rarely as small millerite (NiS) and pentlandite grains (Fig. 10). The presence of gersdorffite in the samples with anomalously high nickel concentrations explains the correlation between Ni, As, and S observed within the pXRF analyses (Fig. 7). These nickel arsenides are concentrated in small quartz and/or carbonate veins and within their selvedge area. Ilmenite grains are also present within the veins and the selvedge. Finally, these veins are associated with the presence of actinolite,

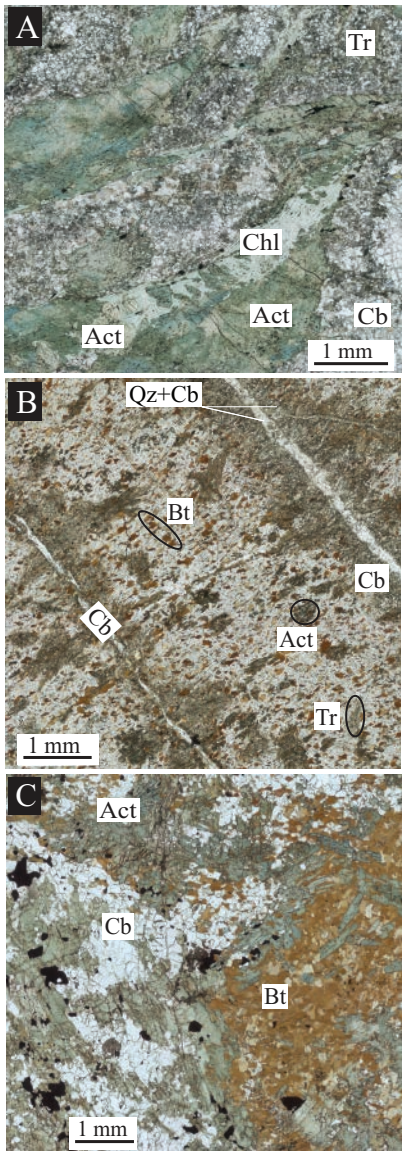

FIG. 8. Photomicrographs of samples representing the "background" composition and textures of the Mount Edwards footwall basalt. (A) Sample DRD738-399, actinolite-tremolite and carbonate metamorphic assemblage with retrograde alteration of the actinolite into chlorite. (B) Sample UMI-04-024-83, the matrix is composed of very fine-grained plagioclase and quartz. Quartz and carbonate veins crosscut the actinolite-tremolite metamorphic assemblage, silicification, and carbonation is present in the selvedges of the different veins. (C) Sample DRD901-548.4, actinolite and carbonate metamorphic assemblage. Biotite formed, probably after actinolite, due to a pervasive potassic alteration syn- and postmetamorphism. Abbreviations: Act = actinolite, Bt = biotite, Cb = carbonate minerals, Chl = chlorite, Qz = quartz, Tr = tremolite.

chlorite, occasionally biotite and hornblende, and rarely serpentine (antigorite and lizardite). A similar alteration type has been described within the Mount Edwards basalt at the Mariners deposit by Goodgame (1997), where nickeline and gersdorffite grains are found within and especially surrounding quartz-calcite veins associated with a weak chlorite-quartz-plagioclase-calcite alteration overprinting earlier biotite which had sometimes been altered to hornblende.

In sample DRD918-358.6, gersdorffite grains are concentrated within a deformed quartz vein, and are associated with pyrrhotite and minor chalcopyrite (Fig. 10B, b and b1). Fibrous chlorite is localized within and particularly along the vein within the selvedge. This vein crosscuts the metamorphosed and altered Mount Edwards footwall basalt (actinolite, biotite, and retrograde chlorite assemblage) and hence is assumed to postdate the main potassic alteration and subsequent retrogression. Similarly, in sample SMD015-W7-674.5, gersdorffite grains are concentrated within a carbonate vein and its actinolite-chlorite-ilmenite rich selvedge area (Fig. 10D, d and d'), which crosscuts the tremolite-biotite-carbonate background assemblage. Within the vein, gersdorffite is associated with the presence of biotite, minor pyrrhotite, and ilmenite. This vein is crosscut and displaced by another late carbonate vein. In sample SMD015-W7- 671.7, the gersdorffite grains are associated with an actinolite-chlorite vein crosscutting the basalt footwall previously altered to a calcite, tremolite, biotite assemblage (Fig. 10E, e and e'). Finally, in samples DRD912-239.5 and DRD738-366.23, quartz-carbonate veins containing the gersdorffite grains are associated with the presence of green hornblende, showing retrogressive alteration to chlorite in places (Fig. 10A, a, C and c). Large gersdorffite grains are also observed in areas of the orebody that have been altered by arsenic-rich fluids. In samples DRD738-371.16, 371.44, and 371.71 (Fig. 11A-C), areas enriched in gersdoffite also show enrichment in chalcopyrite. Gersdorffite grains are clearly late, replacing and altering the primary magmatic assemblage. Gersdorffite grains grow at the boundaries between other grains (mainly pentlandite, pyrrhotite, and chromite) filling intergrain spaces. Many embayments of gersdorffite in pyrrhotite are observed, as well as mantling textures and breakdown of pyrrhotite into gersdoffite (Fig. 11 a, a', b, b', and c).

Mineral chemistry of the nickel arsenides

Six samples were selected for in situ analyses by LA-ICP-MS at the University of Québec in Chicoutimi, Canada. Analyses were collected in order to determine the trace element concentrations, especially PGE concentrations, in the nickel arsenide grains (all results tabulated in Digital Table A5). Two samples (DRD912 and DRD918) contain hydrothermal quartz veins with nickel arsenides, and four others were collected from drill hole DRD738, containing arsenic-enriched portions of the ore.

Nickel arsenides observed within the hydrothermal quartz veins in samples DRD912 and DRD918 are enriched in Pd, Pt, and some Au (Table 1). Palladium is always homogeneously enriched within the nickel arsenide grains (within the lattice of the grains). Platinum behaves in a more heterogeneous way: sample DRD918 is homogeneously enriched in Pt (within the lattice), whereas in sample DRD918, when Pt is present, the spectrum obtained is spikier, probably indicating that Pt might be hosted in inclusions. DRD918 contains between 8.3 and 6.2 ppm Pd and between 0.02 and 31.7 ppm Pt, and DRD912 contains between 0.26 and 16.9 ppm Pd and between 0.03 and 6.9 ppm Pt. Nickel arsenide grains within DRD912 are also enriched in gold with values varying between 0.08 and 6.5 ppm Au. This gold is either present in the lattice of the mineral or as small inclusions. The nickel

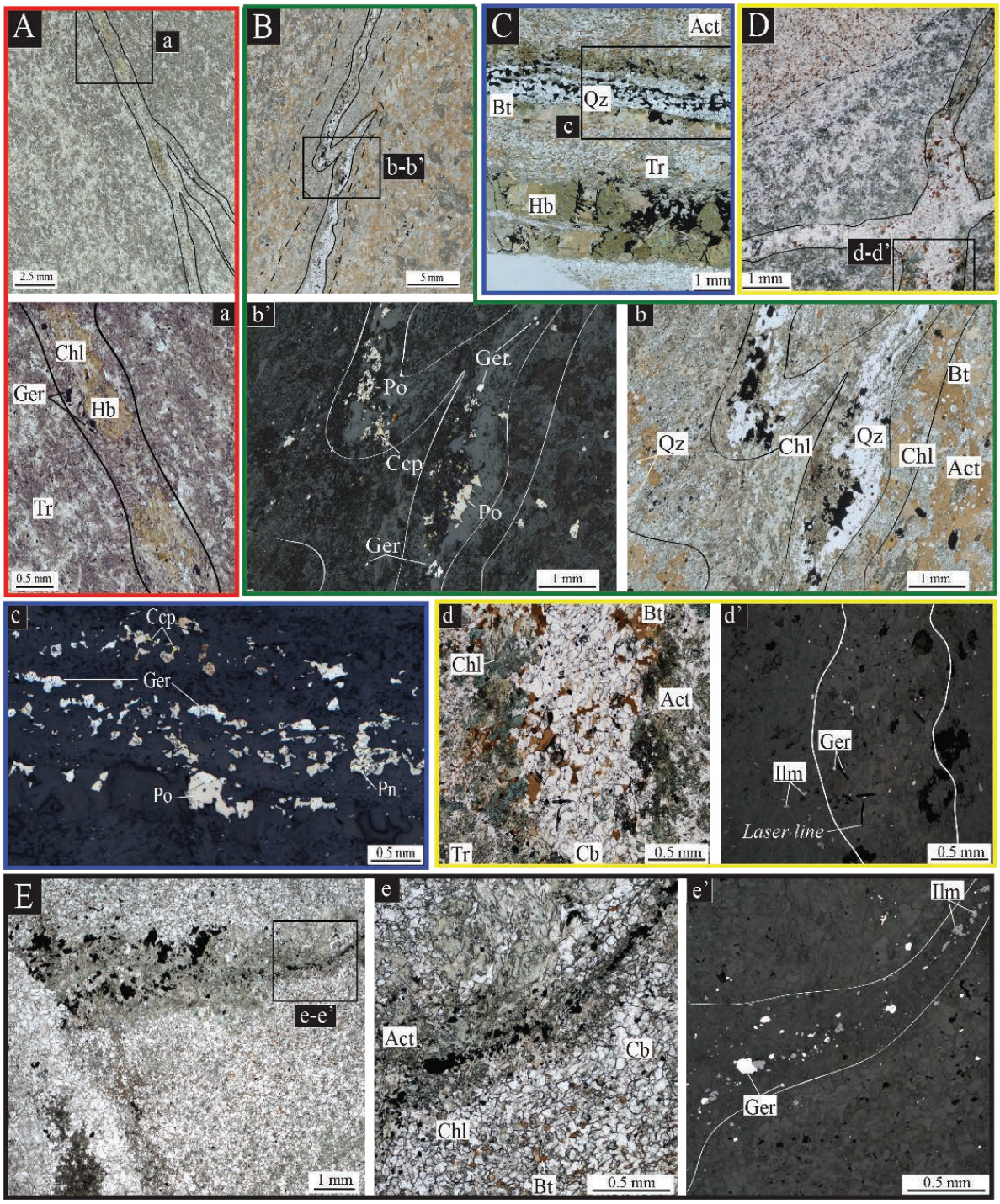

FIG. 9. Photomicrographs of areas analyzed by portable XRF and showing anomalously high nickel concentrations. A) Sample DRD918-358.6, quartz vein cross cutting the Mount Edwards basalt (actinolite/tremolite, chlorite, biotite assemblage). The presence of the vein is associated with a pervasive silicification of the rock as well as chlorite alteration in the selvedges. The vein itself is composed of quartz, chlorite, and sulfides. The sulfide assemblage comprises mainly pyrrhotite and chalcopyrite with nickel arsenides (gersdorffite). a) close up view in transmitted light, a') close-up in reflected light. B) Sample DRD912-239.5, b) close-up in transmitted light. C) Sample DRD738-366.23. Both samples (B and C) contain quartz veins composed of nickel arsenides (gersdorffite) with pyrrhotite and minor chalcopyrite, associated with green hornblende, crosscutting the Mount Edward basalt assemblage of actinolite/tremolite ± biotite. D) Sample SMD015-W7-674.5, carbonate vein containing gersdorffite grains associated with minor pyrrhotite and ilmenite. The vein shows an important actinolite and ilmenite rich selvedge. Photomicrographs d and d' are close-up in transmitted and reflected light of the vein. E) Sample SMD015-W7-671.7, actinolite-chlorite vein rich in gersdorffite and ilmenite. Abbreviations: Act = actinolite, Bt = biotite, Cb = carbonate minerals, Ccp = chalcopyrite, Ger = gersdoffite, Hb = hornblende, Ilm = ilmenite, Pn = pentlandite, Po = pyrrhotite, Qz = quartz, Tr = tremolite.

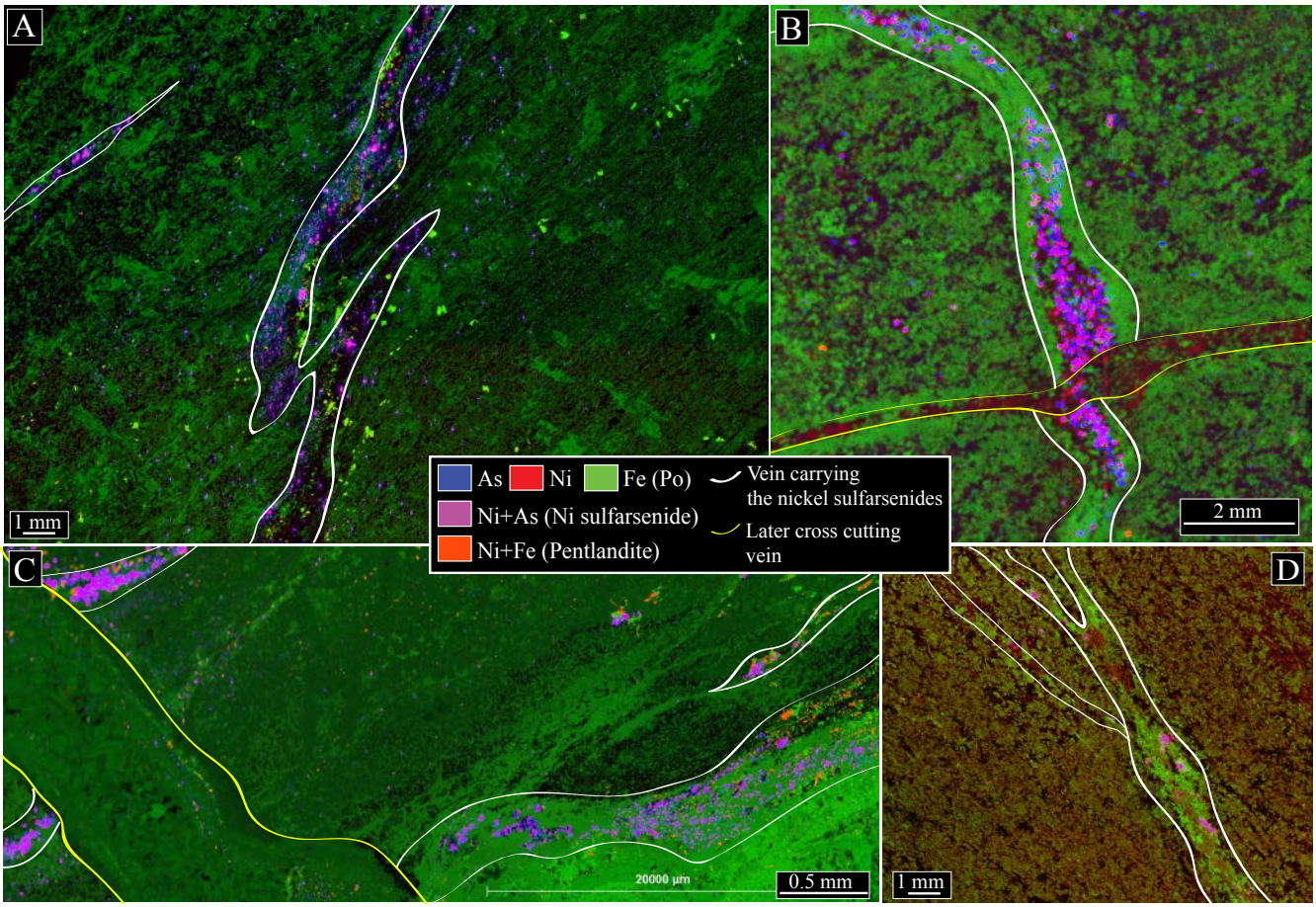

FIG. 10. Three elemental maps of samples DRD918-358.6 (A), SMD015-673.5 (B), SMD015-671.7 (C) and DRD912-239.5 (D) which contain nickel arsenides within small hydrothermal quartz and/or carbonate veins crosscutting the Mount Edwards footwall basalt. These maps were produced using the data collected with either the Maia detector array on the X-ray fluorescence microscopy beamline, at the Australian Synchrotron in Melbourne (maps A and D) or the M4 Bruker TORNADO™ at the Australian Resources Research Center (ARRC) (maps B and C).

arsenides contained within the arsenic-enriched part of the ore (drill hole DRD738) also contain Pd and Pt, in higher concentrations, as well as low levels of IPGE (Ru, Os, Ir) and Rh, but no or very low concentrations of gold. Average contents are 270 ppm Pd, 14 ppm Pt, 22 ppm Ru, 5 ppm Rh, 2 ppm Os, and 1 ppm Ir. Within these grains, a consistent zoning is observed; Pd is enriched within the lattice of the grains, especially in Ni rich areas, whereas all the other PGE are more enriched in Co-rich areas of the grains. These Co-rich areas often form an outer rim. A similar zoning was described within nickel arsenides present in altered areas of the mineralization at the Mariners deposit by Goodgame (1997). At Mariners, arsenic-rich hydrothermal fluids altered the mineralization producing the nucleation of nickeline within pyrrhotite-pentlandite assemblages. This nickeline was then partially to completely replaced by gersdoffite, which in places has cobalt-rich rims as the locus for precious metals (Goodgame, 1997). In summary, at Miitel all hydrothermal nickel arsenides contain Pd and Pt; those formed within the ore also contain IPGE and Rh, and those further away from the ore in hydrothermal veins within the Mount Edwards basalt (close to the contact with the Widgiemooltha komatiite) also contain gold, in the lattice or as small included grains.

Chemistry of the Mount Edwards basalt samples containing anomalously high nickel concentrations

Twenty-six of the contact samples that were analyzed by pXRF were divided in two by lithology (combining visual identification with the pXRF results) and were analyzed for major elements (XRF), trace elements (ICP-MS), and precious metals (lead fire assay) at the Ultra Trace laboratories in Perth, Australia (all results tabulated in App. Table A2). When interpreting the results of these laboratory analyses for Pd, Pt, and Au of samples that contained anomalous nickel and arsenic results with pXRF, it is important to keep in mind that a substantial dilution of the signal created by the hydrothermal vein containing the Pt-, Pd-, and Au-rich nickel arsenides has occurred. Results obtained for the basaltic samples collected away from the ore, both along the footwall contact and away from it, are presented in Figure 12.

On plot A, nine samples containing anomalously high concentrations in Pt and Pd are highlighted, with values ranging from 20 to 140 ppb Pd and 23 to 290 ppb Pt. Typical background values of Pd, Pt, and Au for the Lunnon-type basalt, of which the Mount Edwards basalt is a characteristic example, are respectively 5, 9, and 6 ppb (Said et al., 2011). These

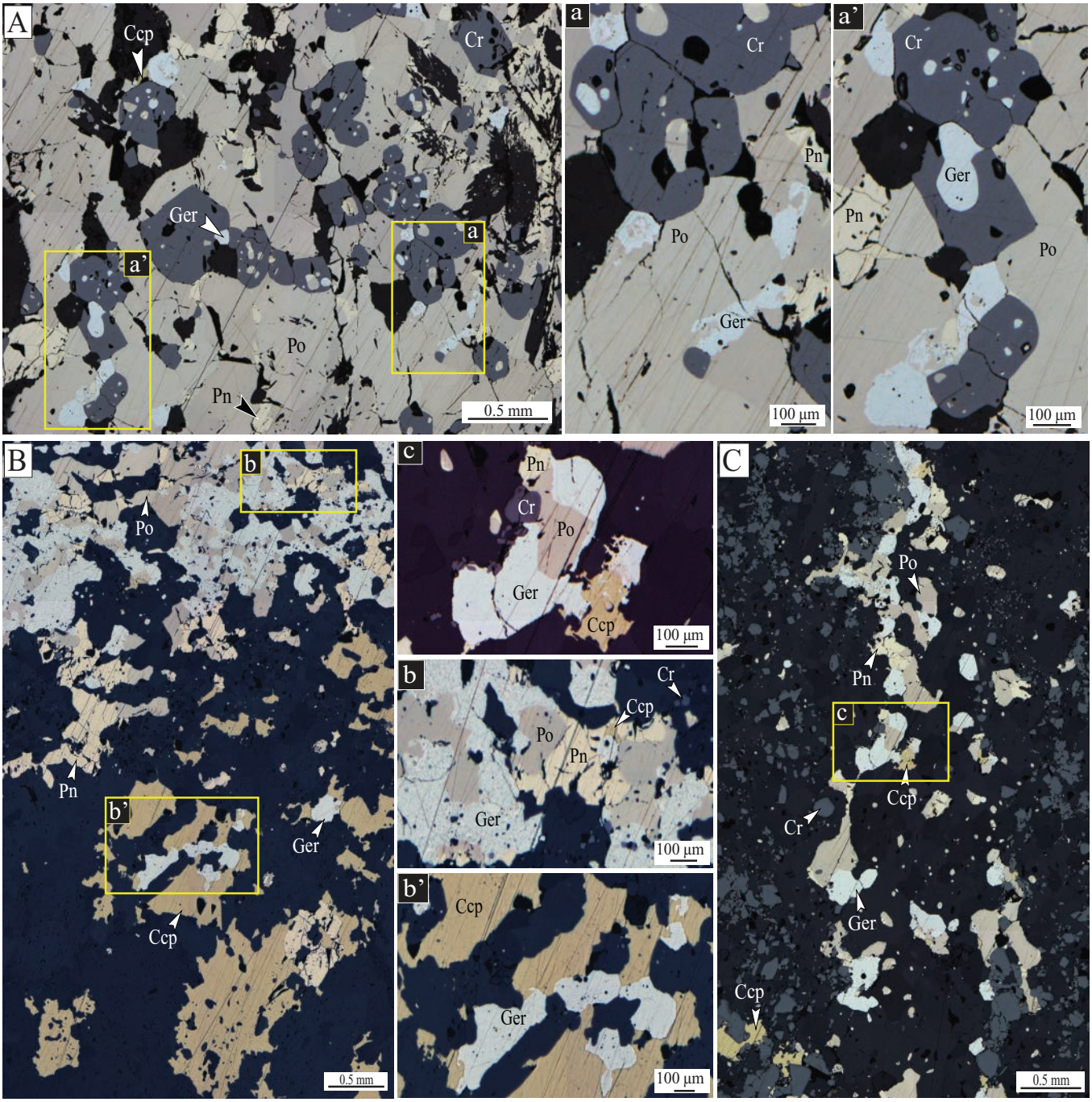

FIG. 11. Photomicrographs of areas of the mineralization altered by As-rich fluids, reflected light. (A) DRD738- 371.51, massive sulfides enriched in gersdorffite, a and a' are close up views of the textural relationships: intergrain infill, embayments of gersdorffite in pyrrhotite. (B) DRD738-371.44, area of the massive sulfides enriched in chalcopyrite and gersdorffite, b and b' are close up views of the textural relationships, embayment of gersdorffite in chalcopyrite and pyrrhotite, intergrain infill, mantling and breakdown of pyrrhotite grains. (C) DRD738-371.16, disseminated sulfides aligned and enriched in gersdorffite grains, within a chromite rich area, c is a close-up view of the textural relationships with the gersdorffite mantling the pyrrhotite-pentlandite-chromite assemblage, especially the pyrrhotite grain that it partially replaced. Abbreviations: Ccp = chalcopyrite, Ger = gersdoffite, Ilm = ilmenite, Pn = pentlandite, Po = pyrrhotite.

samples are particularly anomalous in Pd. Within these nine samples containing anomalous values of Pd and Pt, four also contain elevated concentrations in gold with values ranging from 9 to 120 ppm Au (Fig. 12D, G). In plot A, Pd and Pt display a one-to-one correlation for background level values, but this correlation breaks down when Pd values are above 15 ppb; Pd values are then relatively more elevated than Pt values. Plots B and C demonstrate that elevated Pt and Pd values correspond, in most cases, to samples containing arsenic values above 10 ppm. The same observation can be made

TABLE 1. LA-ICP-MS Results of Analyses Completed on Nickel Arsenide Grains Present Within Hydrothermal Veins in the Footwall Basalt and in Arsenic Altered Area of the Ore

			*Major elements[1] (%)						Trace elements[2] (ppm)											
SAMPLE no.	n		As	Co	Fe	Ni	S	^{107}Ag	^{197}Au	^{65}Cu	^{193}Ir	^{189}Os	^{105}Pd	^{195}Pt	^{103}Rh	^{101}Ru	^{121}Sb	^{82}Se	^{118}Sn	^{66}Zn
DRD912	13	AV	51.86	2.53	8.58	22.47	16.44	4.56	3.94	3.07	0.01	0.01	7.29	2.16	0.03	<DL	227.51	74.80	0.17	6.00
		SD	1.12	0.64	1.90	1.97	0.78	11.28	2.03	5.78	0.01	0.00	5.89	2.09	0.02		387.81	32.93	0.12	6.69
		MD	52.03	2.52	8.99	21.90	16.42	0.79	4.36	1.36	0.01	0.01	5.06	1.75	0.02		121.99	66.43	0.16	3.18
DRD918	9	AV	49.75	2.85	2.63	28.56	17.73	2.19	0.16	0.45	0.02	0.02	34.16	5.39	0.11	<DL	1456.48	165.42	0.22	13.86
		SD	0.09	0.10	0.01	0.05	0.02	3.77	0.07	0.26	0.02	0.02	26.39	10.25	0.11		59.84	9.53	0.12	15.19
		MD	49.79	2.81	2.63	28.58	17.72	1.14	0.14	0.41	0.02	0.01	27.15	1.37	0.07		1440.66	163.49	0.19	8.43
DRD738-371.16	12	AV	48.66	6.03	4.31	24.45	18.69	1.14	0.21	104.48	0.71	2.47	280.15	7.12	1.92	<DL	386.43	81.49	0.26	62.12
		SD	0.15	0.43	0.13	0.36	0.09	1.05	0.05	194.39	0.64	2.54	35.17	5.62	1.63		18.34	3.03	0.09	137.86
		MD	48.69	5.75	4.30	24.61	18.65	0.64	0.22	2.24	0.72	1.92	291.10	6.30	1.53		386.73	81.18	0.27	15.81
DRD738-371.44	7	AV	48.34	8.16	4.74	22.25	18.91	0.61	7.42	141.63	0.65	1.74	93.95	0.54	0.45	7.25	245.04	60.98	0.32	48.47
		SD	0.05	0.72	0.07	0.69	0.05	0.38	19.01	357.66	0.42	1.77	87.88	0.31	0.19	0.62	43.00	6.00	0.08	43.10
		MD	48.32	8.42	4.74	21.97	18.89	0.54	0.27	2.28	0.66	1.21	27.17	0.45	0.46	7.25	218.58	57.99	0.35	36.25
DRD738-371.51A	9	AV	47.56	11.57	4.82	18.90	18.90	31.02	0.51	296.69	7.06	24.46	232.44	215.84	41.50	59.74	301.90	99.71	0.37	7.40
		SD	1.05	7.20	0.34	6.44	0.44	26.78	0.27	597.39	5.82	14.43	86.53	79.32	20.49	30.81	45.08	19.03	0.16	13.72
		MD	48.03	6.91	4.72	22.47	18.55	22.36	0.52	15.36	5.83	17.39	277.11	196.03	36.62	50.67	314.41	104.44	0.38	1.77
DRD738-371.51B	17	AV	48.24	7.14	4.69	23.22	18.80	2.89	0.25	600.19	4.58	10.31	250.78	112.93	19.02	27.03	287.97	88.24	0.48	31.60
		SD	0.58	3.61	0.28	3.33	0.25	2.86	0.12	2106.70	9.23	20.25	94.28	139.80	25.39	34.69	40.31	14.96	0.18	73.89
		MD	48.20	6.40	4.57	23.70	18.73	2.86	0.23	7.58	0.77	2.44	275.36	81.54	12.04	9.19	293.61	94.84	0.43	5.86

AV = average, MD = median, n = number of analyses, SD = standard deviation on n analyses, <DL = below detection limit
[1] Data obtained with microprobe analyses
[2] Data obtained with LA-ICP-MS analyses

in plots E, F, and G, where elevated Pd, Pt, and Au values correspond in most cases to samples containing more than 200 ppm Ni. However, samples containing elevated Pd and Pt values but not anomalous values in Ni and As are also present. Here, nickel values above 200 ppm (median + 2 · SD) are considered anomalous since the calculated background for the Mount Edwards basalt obtained with laboratory analyses, as detailed above, is 127 ± 32 ppm. No significant correlation is observed between Pd and S (Fig. 12H).

3-D Data Presentation

The results presented above establish the presence of microscale Ni-As-Pt-Pt-rich quartz and/or carbonate veins containing Pd-Pt-enriched gersdorffite in the Mount Edwards footwall basalt, close to the contact with the Widgiemooltha komatiites. In order to establish the spatial relationship between these veins and the regional scale arsenic metasomatism (Cairns et al., 2003), a 3-D model was compiled, combining the distribution of the arsenic in the Miitel system from the assay database of Mincor Resources NL with the structural information summarized above (Fig. 13A), the location of the Ni-As-Pt-Pd–enriched veinlets and the distribution of anomalous whole-rock Pt-Pd results (Fig. 12).

On the first model of the distribution of arsenic (isotropic model, Fig. 13A), a NNE-SSW trend similar to the one described in Cairns et al. (2003) can be observed, and is incorporated in the second model as a structural trend (Fig. 13B). Both models are biased by the concentration of data points along the mineralized channel, but a trend is still clear. The high arsenic concentrations (from 100 to over 2,500 ppm) are orientated along a shallow dipping SSW-NNE trend, crosscutting the orientation of the mineralized channel. This trend is interpreted as resulting from the presence of S-SSW shallow-dipping splay structures, related to the D_4 event, along which arsenic-rich hydrothermal fluids circulated.

Figure 13C is a long section along the footwall contact showing the distribution of arsenic concentrations on that contact, as well as the location of Ni-As-Pd-Pt-enriched veinlets and high Pd-Pt samples. There is a close spatial relationship between the distribution of the regional metasomatic enrichment in arsenic and the distribution of the basalt samples containing high Ni, As, Pd, and Pt concentrations. The Ni-As-Pd-Pt-enriched veinlets are located within decimeters of the contact with the komatiites, in arsenic enriched areas, and in the prolongation of the orebodies (Fig. 13C). The distance between the farthest samples containing anomalously high Ni, As, Pd, and Pt concentrations and the ore is 250 m (white arrow in Fig. 13C). Moreover, one can observe the important difference between the size of the arsenic overprint close to the contact vertically above and below the massive nickel sulfides.

Discussion

This study has highlighted anomalously elevated nickel concentrations (pXRF) within the footwall basalt, up to a meter away from the contact with the Widgiemooltha mineralized komatiites, which extends at least 250 m away from the closest nickel sulfide orebody. Samples creating these anomalous nickel values do not contain any visible nickel sulfides that could account for the high nickel concentrations, no massive nickel sulfide bodies are in close contact, and there is

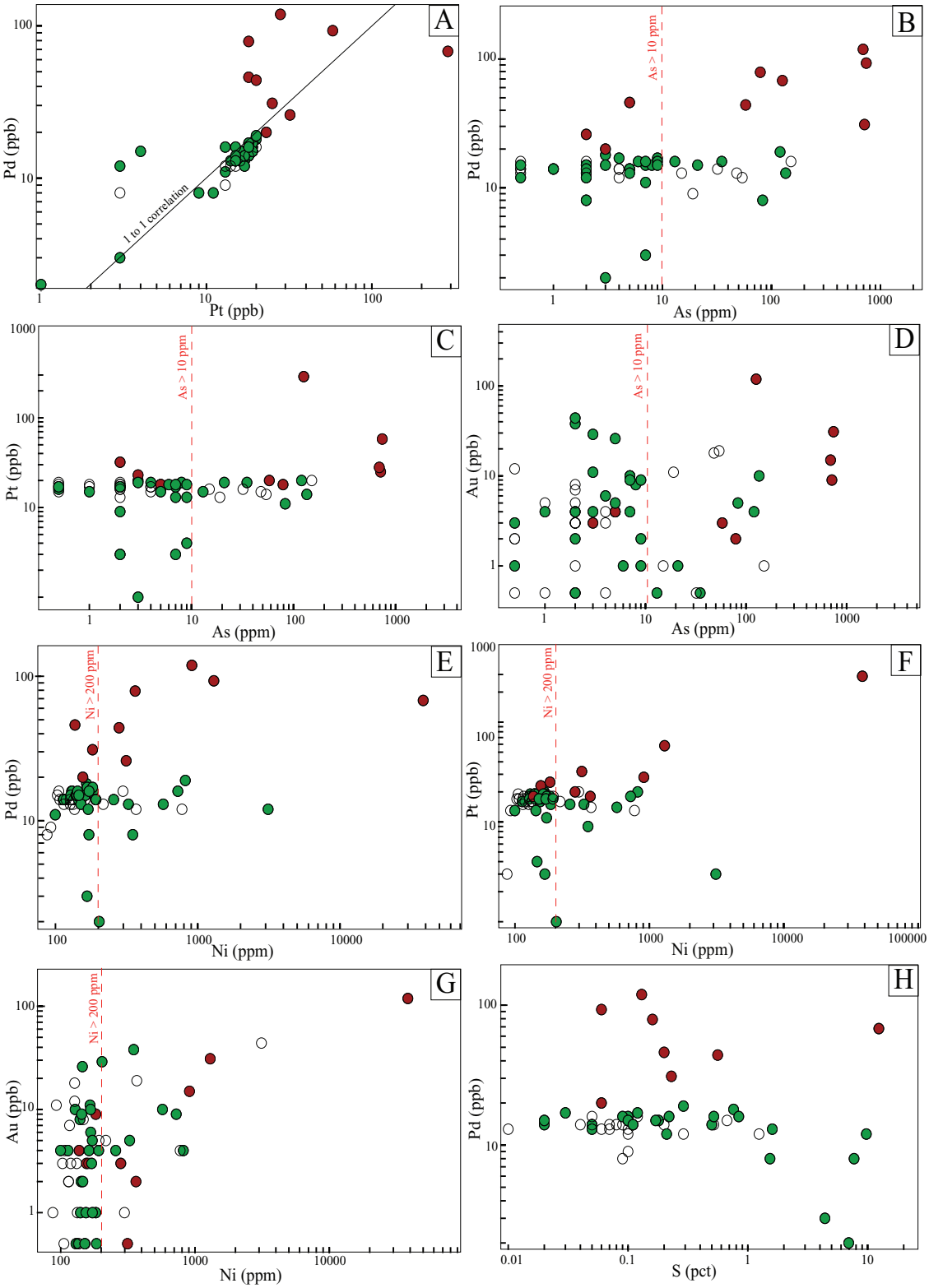

FIG. 12. XY plots of the geochemical results from the Ultra Trace laboratories in Perth. The samples represented in these plots are all basalts collected close at the contact between the Mount Edwards basalt and the Widgiemooltha komatiites, all of which had previously been analyzed by pXRF (multiple pXRF analyses for every sample sent to the laboratory). Values of nickel greater than 200 ppm are considered anomalous (200 ppm = median (of analyses on background samples) + 2 × the standard deviation).

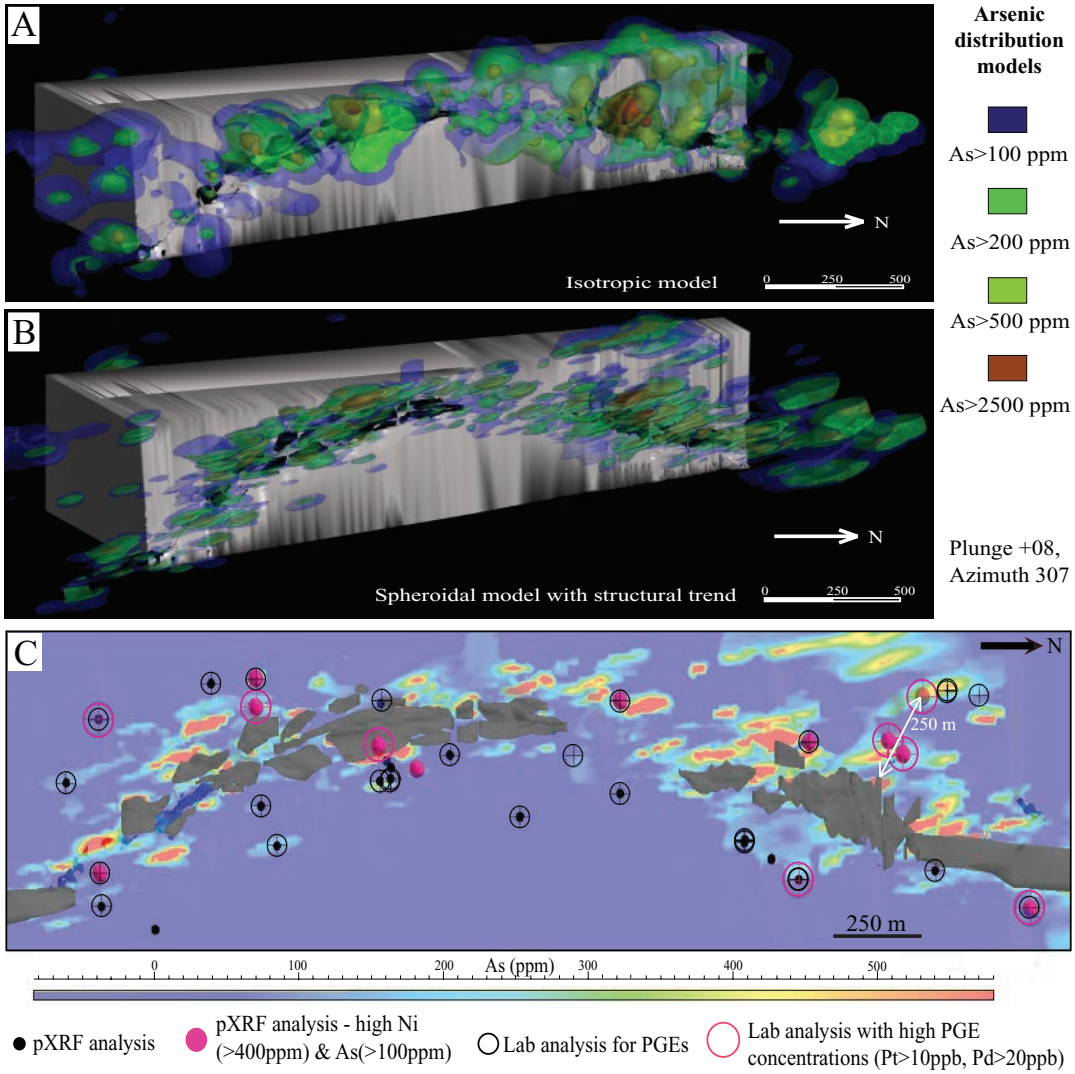

FIG. 13. (A) Isotropic and (B) spheroidal with structural trend 3-D model of the distribution of arsenic concentrations within the Miitel deposit. The geology is viewed from the same angle as in Figure 3 and the nickel resources in the 3-D model are defined by a 1% nickel cutoff. (C) Perspective view from gOcad® of a long section through the 3-D model of the Miitel deposit. This image combines (1) distribution of the arsenic in ppm at the contact between the basalt and the komatiites (model derived using Leapfrog®), (2) location of pXRF analyses showing anomalously high nickel and arsenic concentrations, and (3) location of lab PGE analyses highlighting samples enriched in PGE.

no correlation between S and PGE. Therefore, mechanical remobilization of nickel-enriched sulfide into the basalt cannot account for the anomalism. It is more likely that nickel has been remobilized by hydrothermal fluids and reincorporated within a mineral phase deposited by or reacting with these fluids. The main nickel-hosting phase in these samples was identified by petrography, SEM-EDS, and elemental mapping, as gersdorffite (NiAsS) concentrated within small quartz and/or carbonate veins, suggesting that the nickel has been remobilized and transported by arsenic-rich hydrothermal fluids.

Source of the nickel

It has been proposed in the previous section that nickel enrichment resulted from the remobilization of metals by arsenic-rich hydrothermal fluids, but a question remains: where is the nickel coming from? There are three possible sources of nickel for these nickel arsenide-rich veins: (1) derivation from deep or distal sources on regional scale via the hydrothermal fluids themselves, (2) massive nickel sulfides, or (3) the Widgiemooltha komatiites. Considering the data on basalt samples at the contact with the Widgiemooltha komatiites on a regional scale (batch 2), it has been noted that multiple samples show very elevated concentrations in arsenic, implying alteration by regionally derived arsenic rich hydrothermal fluids. However, none of these samples contains anomalous concentrations of nickel (max. value of 294 ppm Ni). Therefore, it is unlikely that nickel has been derived distally via the As-rich fluids, a conclusion consistent with the general lack of nickel enrichment found with Archean lode Au deposits known to be associated with As-enriched fluids (Smith, 1984; McCuaig, 1998). By similar reasoning, the absence of nickel enrichment in As-enriched basalt at the komatiite contact within most of

the batch 2 regional samples also indicates that the immediately adjacent, sulfide-free Widgiemooltha komatiite is not the source of the anomalous nickel.

The remaining possible source of nickel is the Miitel orebody. The distinguishing characteristic of the massive nickel sulfides, distinct from host komatiite, is their enrichment in PGE. The unmineralized komatiites are composed of olivine cumulates, which on the basis of the extensive database of Fiorentini et al. (2010) would be expected to contain no more than 2 ppb each of Pd and Pt. Similar values are typical of the Lunnon-type basalt (avg of 5 ppb; Said et al., 2011) of which the Mount Edwards basalt is a typical example. Details of PGE contents of Miitel ores are unavailable, but massive ores of the Kambalda-Widgiemooltha area typically have Pd and Pt contents in the range 500 to 2,000 ppb (Barnes, 2006a). Laboratory assay results and PGE analyses of the Ni-As mineral phases themselves confirm the association between anomalously high Ni-As and high Pd, Pt, and Au concentrations, confirming that the processes of remobilization of Ni and PGE are intimately linked. On this basis, and given the spatial association of the Ni-As-Pd-Pt anomalism with proximity to the ores, and absence of this anomalism in the more distal samples, it is concluded that the Miitel ore is the most likely source of the nickel and PGE components, with the arsenic being derived from the regional fluids. The association of Pd and Pt, but lack of IPGE and Rh, in the NiAs-bearing veinlets reflects the fact that, of the six PGE, Pd and particularly Pt are the most mobile in hydrothermal fluids (Wood, 2002; Hanley et al., 2005; Barnes and Liu, 2012). Moreover, the generally higher concentration of Pd compare to Pt is probably a result of the difference in mobility of these two elements (Wood, 2002; Hanley et al., 2005; Barnes and Liu, 2012).

Ni, Co, Pd, Pt transport mechanism

The understanding of Ni, Co, Pd, and Pt transport and deposition relies on the knowledge of the aqueous complexes responsible for their solubility in hydrothermal fluids, and on the availability of thermodynamic properties for each relevant species as a function of pressure, temperature, and fluid chemistry (Seward and Barnes, 1997; Brugger et al., 2010; Barnes and Liu, 2012; Tian et al., 2012). Studies on the behavior of Ni, Co, Pd, and Pt in hydrothermal fluids, which are still limited, show an increasing solubility with sulfur contents and the formation of bisulfide complexes (Wood et al., 1989; McKibben et al., 1990; Gammons et al., 1993; Pan and Wood, 1994; Tagirov and Baranova, 2009; Barnes and Liu, 2012), and with chloride contents and formation of chloride complexes (Sassani and Shock, 1990, 1998; Gammons et al., 1992, 1993; Wood et al., 1992; Liu et al., 2011, 2012; Barnes and Liu, 2012; Tian et al., 2012). It is observed that the arsenides in the hydrothermal halo surrounding the Miitel orebody are enriched in Ni compared to Co. This enrichment could be interpreted as an indication of the higher solubility of Co in arsenic-rich fluids, as it is the case in chloride-rich fluids (Liu et al., 2011), whereby Co remains in solution while Ni and Pd are deposited as nickel arsenides. However, this hypothesis cannot be fully tested, as there are no available data on the behavior of Ni, Co, Pd, and Pt in arsenic-rich hydrothermal fluids.

The transport and deposition of Ni and Pd within the Mount Edwards basalt in close proximity to the footwall contact extends at least 250 m away from the massive sulfides. The size of the resulting halo depends on the stability and solubility of the complexes formed by Ni and Pd within the arsenic-rich fluids. More detailed understanding awaits new experimental and thermodynamic data on speciation and solubility of such complexes.

Geometry of the hydrothermal halo

Cairns et al. (2003) interpreted the distribution of high arsenic values at Miitel as being epigenetic, overprinting the nickel sulfide ore during deformation. Petrographic study of sample DRD738-371 confirms this observation. This enrichment in arsenic is thought to have been introduced into the system by west dipping shear zones and associated shallower S-SSW shallow dipping splay-structures. Arsenic concentrations are especially elevated at the intersection of these structures with the ore, since massive sulfides are the source of sulfur, nickel, and iron that form the arsenic-bearing minerals, gersdorffite (NiAsS) and nickeline (NiAs). Moreover, these fluids could be similar to the ones associated with the genesis of world-class orogenic gold deposits, such as the Mount at Widgiemooltha, 80 km south of Coolgardie, with over 300,000 oz of gold (ASX announcement, Focus Minerals (2011)), or those of the St Ives Camp 30 km to the NNE. This association with a regional orogenic gold event explains the presence of gold within the hydrothermal nickel arsenides (especially sample DRD912 with values of about 5 ppm Au; LA-ICP-MS results; Table 1). Another line of evidence is in the geometry of the arsenic distribution along the footwall contact (Fig. 13). High arsenic concentrations are more abundant and spread over larger distances above than below the mineralized channel. This observation could indicate that the hydrothermal fluids were moving upward.

Source of the arsenic

As stated above, the arsenic-rich fluids that circulated through the system at Miitel could be associated with the regional orogenic gold event that Groves et al. (2003) linked with the occurrence of crustal fluids. However, few crustal rock types can represent a realistic source of arsenic. Boyle and Jonasson (1973) studied the global distribution of arsenic and its abundance in various rock types. According to the database that they assembled, the most endowed source of arsenic in the regional setting, where the Miitel deposit is located, would comprise interflow sediments made up of black shales, schists and chert horizons. The composition of these interflow sediments has been studied by Bavinton (1981), but their arsenic content was not reported. Samples from the Cobalt area, Ontario, of a similar Archean lithology yielded an average concentration of 80 ppm As (Boyle and Jonasson, 1973). Furthermore, later studies by Quinby-Hunt et al. (1989) and Ketris and Yudovich (2009) evaluating the world-wide composition of shales respectively obtained average concentrations of 29 and 30 ppm As for carbonaceous shales, representing about 16 times the normal crustal average, considering that most crustal rocks contain only 1 to 4 ppm As (Large et al., 2011). Therefore, at Miitel there is enough crustal arsenic available to produce the arsenic-rich hydrothermal fluids responsible for the observed halo.

Practical Application to Exploration

The first step in using this Ni-As-Pd-Pt geochemical halo as an exploration tool is the routine collection of Ni and As assays in country rocks along contacts and major structures, in addition to the normal practice of analyzing these elements in ultramafic rocks only. Once arsenic-bearing structures (faults, contacts, and foliation) are identified, and background concentrations of the different rock types, in both nickel and arsenic, have been determined, a 3-D representation of anomalous Ni-As samples could identify an expanded halo around the orebody. At Miitel, there is a close relationship between the geometry of the arsenic overprint and the geochemistry of the geochemical halo created around the massive nickel sulfides (Fig. 14). High arsenic and nickel areas represent a positive signature indicating proximity to nickel sulfides, while high arsenic and low nickel represent low prospectivity areas. Importantly, a combined low arsenic and low nickel signal would be considered as neutral, on the grounds that Ni remobilization is only observed within zones of As enrichment. Coincident high Ni and As samples would warrant follow up with PGE assays; Pb fire assay with ICP-MS finish for Pt, Pd, and Au is the recommended method, with periodic quality control checks using a nickel sulfide fire assay preconcentration step.

In the case of the Miitel case study, pXRF was used as the main tool to identify the geochemical halo. Depending on the tool used, the methodology and the values used as "background" will differ. Portable XRF is the ideal tool to detect small features, such as the NiAs-enriched hydrothermal veins surrounding the Miitel deposit, but one must keep in mind that it will only give data over a very small sample of rock. To effectively use pXRF, multiple readings must be collected and highest values (of nickel and arsenic) will then be used to define the shape and extent of the geochemical halo. Moreover, the "background" value will be more elevated than for laboratory analyses (e.g. 249 ± 75 ppm is the background

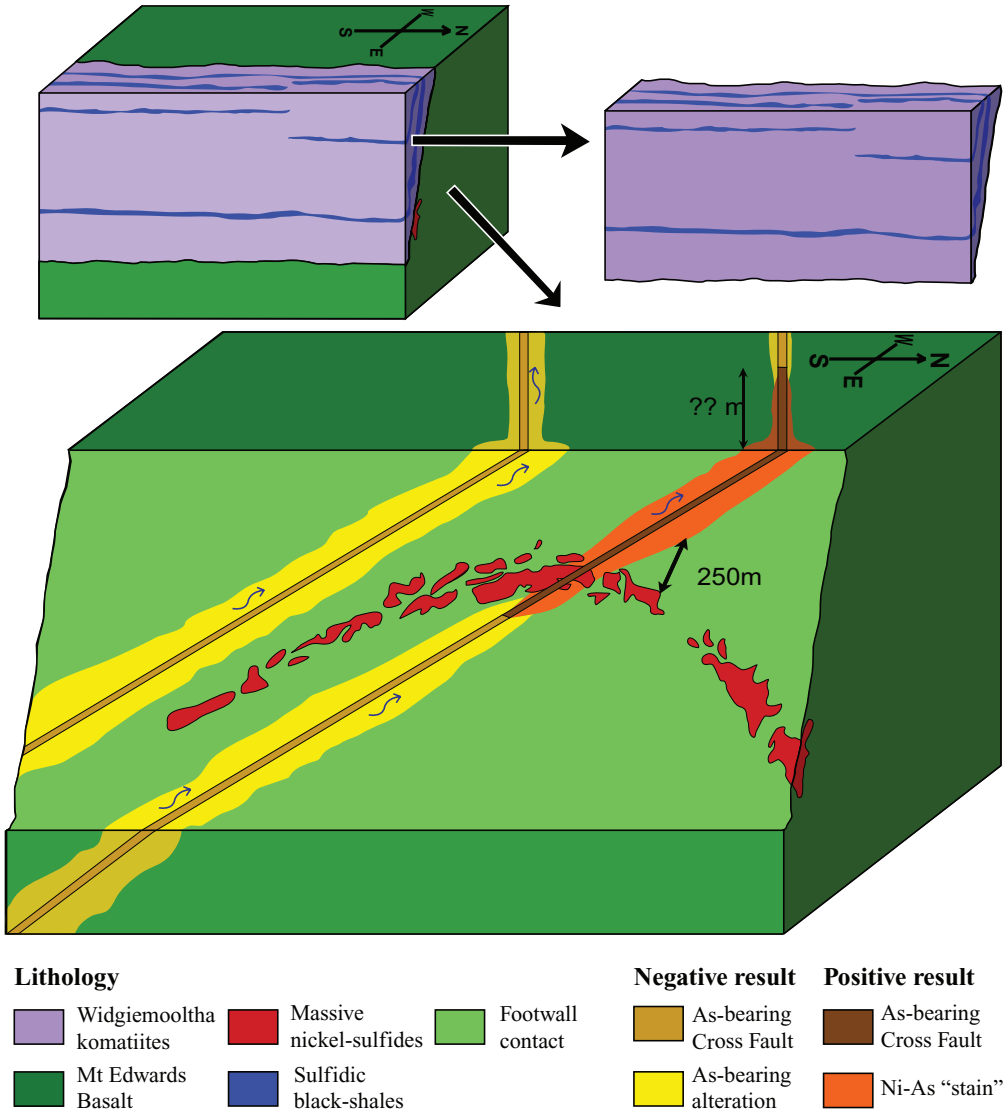

FIG. 14. 3-D block model of the Miitel system showing the possible application of the Ni-As-Pd-Pt geochemical halo to exploration targeting for nickel sulfides.

nickel value for the Mount Edwards basalt with pXRF, and values above 400 ppm (median + 2 · SD) are considered anomalous. If using laboratory analyses (assay databases), one must keep in mind that a small feature such as those observed at Miitel will give a diluted signal, and the values considered as anomalous will be lower (e.g., background of 127 ± 32 ppm Ni for the Mount Edwards basalt, and values above 200 ppm considered anomalous).

The size of the geochemical halo identified around the Miitel ore is on the same scale as that identified from primary Pd and Pt enrichment due to sulfide enrichment in host komatiites at Maggie Hays (Heggie et al., 2012) and Long-Victor (Kambalda; Barnes et al., 2013). The potential for the hydrothermal halo to operate where the primary PGE halo cannot is in settings where sulfide orebodies have been tectonically separated from their host rocks, a common situation in highly deformed terranes (Barnes, 2006b; Layton-Matthews et al., 2007). Investigation of Ni-As-Pd-Pt haloes in polydeformed terranes is a new addition to the exploration toolkit, especially useful when considering its very low potential for false positive findings. This geochemical tool represents a critical complementary technology, and associated with identified EM anomalies, noted for high false positive rates, it can help prioritizing targets.

For exploration purposes, investigation of a possible Ni-As-Pd-Pt geochemical halo would be useful. The presence of Pd-enriched nickel bearing arsenide phases in sheared rocks within prospective terrains may be an effective "near miss" indicator for nickel sulfides in a range of settings.

Arsenic has a deleterious effect during processing of contaminated ore. The geochemical exploration tool described here could therefore be seen as having limited potential, in that it might lead to the discovery of orebodies of low value. This is not necessarily the case. In fact, many economic nickel deposits contain arsenic-enriched areas, due to magmatic and/or metasomatic processes (e.g. Mariners, Miitel). Generally, arsenic-contaminated areas occur along defined faults and shear zones and affect only restricted parts of the deposit. Therefore, it is common practice to carry out a careful monitoring of arsenic concentrations, combined with a good understanding of associated structural controls in order to ensure that these deposits can be mined and exploited economically.

Conclusions

A cryptic Ni-As-Pd-Pt geochemical halo is present around the Miitel orebody, formed by the late circulation of arsenic-rich hydrothermal fluids (Fig. 13). These arsenic-rich fluids are interpreted as flowing upward, mainly along the footwall contact and late SSW shallow-dipping crosscutting splay structures. These hydrothermal fluids collected nickel and PGE (mainly Pd and Pt) from the massive nickel sulfides, transported them, and redeposited them within small quartz and/or carbonate veins close to the footwall contact. This geochemical halo extends along the basal contact at least 250 m away from the ore, and the larger coverage of the arsenic rich metasomatism (As >100 ppm), especially along the D_4 structures, outside the limit of drilling availability, could infer an even wider NiAs-PGE halo. This cannot currently be tested at Miitel. The extent of this NiAs-PGE halo could be larger than any geochemical tool currently in use for nickel sulfide exploration targeting.

Ni-As-Pd-Pt geochemical haloes, similar to those described in this paper, could potentially exist around any type of magmatic nickel sulfide mineral system that has undergone a phase of arsenic metasomatism, especially if these arsenic-rich hydrothermal fluids can be linked to an orogenic gold mineralizing event.

This study provides an example of a practical application of portable XRF on drill core surfaces as a near-mine exploration tool. Portable XRF allows the rapid, cost effective, and reliable detection of the range of elements (Ni, As, S, Cr, Ti, Zr) needed to detect the Ni-As-Pd-Pt geochemical halo described here. Moreover, the fact that pXRF only allows the analysis of a small portion of the rock (1.5cm^2), making it sensitive to cm-scale heterogeneities—often seen as an issue regarding representativeness of the data—is in this case its main advantage, allowing us to detect the small veins containing the nickel arsenides that might be missed with traditional laboratory XRF analyses.

Acknowledgments

Financial support for this research was provided by MERIWA (project #M413), BHP Billiton Nickel West, Mincor Resources NL, and First Quantum Minerals Ltd. This project is part of an ongoing PhD research project at UWA and the SIRF scholarship of the University of Western Australia and the MERIWA research grant are greatly appreciated. Mincor Resources NL is acknowledged for providing on site access and samples. We would like to thank Louise Fisher and Stefano Caruso for their help collecting, processing, and interpreting the portable XRF data, June Hill for assistance with data interpolation using Leapfrog® software, and Adam Bath and Belinda Godel for extremely helpful reviews of an early draft. The element maps were collected using the Maia Detector on the X-ray fluorescence microscopy beamline on the Australian Synchrotron in Clayton, Victoria, and we thank David Paterson and Kathryn Spiers for their patience and expertise when supervising this work. Sarah-Jane Barnes, Sarah Dare, and Danny Savard are thanked for their assistance with the use of the LA-ICP-MS at UQAC, Canada. This is contribution 463 from the ARC Centre of Excellence for Core to Crust Fluid System (http://ccfs.mq.edu.au) and an output from the CSIRO Minerals Down Under National Research Flagship. Jacob Hanley and Michel Houlé are thanked for their valuable review of this manuscript.

REFERENCES

Archibald, D.A., Bettenay, L.F., Binns, R.A., Groves, D.I., and Gunthorpe, R.J., 1978, The evolution of Archaean greenstone terranes, Eastern Goldfields province, Western Australia: Precambrian Research, v. 6, p. 147–163.

Barnes, S.J., 2006a, Komatiite-hosted nickel-sulfide deposits: Geology, geochemistry, and genesis: Society of Economic Geologists Special Publication 13, p. 51–118.

——2006b, Komatiites: Petrology, volcanology, metamorphism and geochemistry: Society of Economic Geologists Special Publication 13, p. 13–49.

Barnes, S.J., and Brand, N.W., 1999, The distribution of Cr, Ni, and chromite in komatiites, and application to exploration for komatiite-hosted nickel sulfide deposits: Economic Geology, v. 94, p. 129–132.

Barnes, S.J., and Fiorentini, M.L., 2012, Komatiite magmas and sulfide nickel deposits: A comparison of variably endowed Archean terranes: Economic Geology, v. 107, p. 755–780.

Barnes, S.J., and Hill, R.E.T., 2000, Metamorphism of komatiite hosted nickel sulfide deposits, *in* Spry, P.G., Marshall, B., and Vokes, F.M., eds., Metamorphosed and metamorphogenic ore deposits: Reviews in Economic Geology, v. 11, p. 203–216.

Barnes, S.J., and Liu, W., 2012, Pt and Pd mobility in hydrothermal fluids: Evidence from komatiites and from thermodynamic modelling: Ore Geology Reviews, v. 44, p. 49–58. DOI: 10.1016/j.oregeorev.2011.08.004.

Barnes, S.J., Hill, R.E.T., Perring, C.S., and Dowling, S.E., 2004, Lithogeochemical exploration for komatiite-associated Ni-sulfide deposits: Strategies and limitations: Mineralogy and Petrology, v. 82, p. 259–293. DOI: 10.1007/s00710-004-0051-7.

Barnes, S.J., Van Kranendonk, M.J., and Sonntag, I., 2012, Geochemistry and tectonic setting of basalts from the Eastern Goldfields Superterrane: Australian Journal of Earth Sciences, v. 59, p. 707–735. DOI: 10.1080/08120099.2012.687398.

Barnes, S.J., Heggie, G.J., and Fiorentini, M.L., 2013, Spatial variation in platinum group element concentrations in ore-bearing komatiite at the Long-Victor deposit, Kambalda dome, Western Australia: Enlarging the footprint of nickel sulfide orebodies: Economic Geology, v. 108, p. 913–933. DOI: 10.2113/econgeo.108.5.913.

Bavinton, O.A., 1981, The nature of sulfidic metasediments at Kambalda and their broad relationships with associated ultramafic rocks and nickel ores: Economic Geology, v. 76, p. 1606–1628.

Begg, G.C., Hronsky, J.A.M., Arndt, N.T., Griffin, W.L., O'Reilly, S.Y., and Hayward, N., 2010, Lithospheric, cratonic, and geodynamic setting of Ni-Cu-PGE sulfide deposits: Economic Geology, v. 105, p. 1057–1070.

Bleeker, W., 1990, Evolution of the Thompson nickel belt and its nickel deposits: Unpublished Ph.D. thesis, Manitoba, Canada, University of New Brunswick, 444 p.

Blewett, R.S., Czarnota, K., and Henson, P.A., 2010, Structural-event framework for the eastern Yilgarn craton, Western Australia, and its implications for orogenic gold: Precambrian Research, v. 183, p. 203–229. DOI: 10.1016/j.precamres.2010.04.004.

Boyle, R.W., and Jonasson, I.R., 1973, The geochemistry of arsenic and its use as an indicator element in geochemical prospecting: Journal of Geochemical Exploration, v. 2, p. 251–296.

Brugger, J., Pring, A., Reith, F., Ryan, C., Etschmann, B., Liu, W., O'Neill, B., and Ngothai, Y., 2010, Probing ore deposits formation: New insights and challenges from synchrotron and neutron studies: Radiation Physics and Chemistry, v. 79, p. 151–161. DOI: 10.1016/j.radphyschem.2009.03.071.

Burnham, O.M., Halden, N., Layton-Matthews, D., Lesher, C.M., Liwanag, J., Heaman, L., Hulbert, L., Machado, N., Michalak, D., Pacey, M., Peck, D., Potrel, A., Theyer, P., Toope, K., and Zwanzig, H., 2003, Geology, stratigraphy, petrogenesis, and metallogenesis of the Thompson nickel belt, Manitoba: Sudbury, Mineral Exploration Research Centre, Camiro Project 97E-02 final report, 444 p.

Cairns, C.P., Mapleson, D.B., Bewsher, A.W., and McCuaig, T.C., 2003, Understanding the structural controls on arsenic mineralisation and ore distribution at the Miitel nickel mine, Widgiemooltha, Western Australia, *in* Dominy, S., ed., Fifth International Mining Geology Conference: Bendigo, Victoria, AusIMM.

Cassidy, K.F., Champion, D.C., Krapez, B., Barley, M.E., Brown, S.J.A., Blewett, R.S., Groenewald, P.B., and Tyler, I.M., 2006, A revised geological framework for the Yilgarn craton: Western Australia Geological Survey, Department of Industry and Resources, Report, 14 p.

Duuring, P., Bleeker, W., and Beresford, S.W., 2007, Structural modification of the komatiite-associated Harmony nickel sulfide deposit, Leinster, Western Australia: Economic Geology, v. 102, p. 277–297.

Fahlquist, L.S., and Popp, R.K., 1989, The effect of NaCl on bunsenite solubility and Ni-complexing in supercritical aqueous fluids: Geochimica et Cosmochimica Acta, v. 53, p. 989–995.

Fiorentini, M.L., Barnes, S.J., Lesher, C.M., Heggie, G.J., Keays, R.R., and Burnham, O.M., 2010, Platinum group element geochemistry of mineralized and nonmineralized komatiites and basalts: Economic Geology, v. 105, p. 795–823.

Fiorentini, M.L., Beresford, S., Barley, M.E., Duuring, P., Bekker, A., Rosengren, N., Cas, R., and Hronsky, J., 2012, District to camp controls on the genesis of komatiite-hosted nickel sulfide deposits, Agnew-Wiluna greenstone belt, Western Autralia: Insights from the multiple sulfur isotopes: Economic Geology, v. 107, p. 781–796.

Gammons, C.H., Bloom, M.S., and Yu, Y., 1992, Experimental investigation of the hydrothermal geochemistry of platinum and palladium: I. Solubility of platinum and palladium sulfide minerals in $NaCl/H_2SO_4$ solutions at 300°C: Geochimica et Cosmochimica Acta, v. 56, p. 3881–3894.

Gammons, C.H., Yu, Y., and Bloom, M.S., 1993, Experimental investigation of the hydrothermal geochemistry of platinum and palladium: III. The solubility of Ag-Pd alloy + AgCl in NaCl/HCl solutions at 300°C: Geochimica et Cosmochimica Acta, v. 57, p. 2469–2479.

González-Álvarez, I., Pirajno, F., and Kerrich, R., 2013a, Hydrothermal nickel deposits: Secular variation and diversity: Ore Geology Reviews, v. 52, p. 1–3. DOI: 10.1016/j.oregeorev.2012.11.006.

González-Álvarez, I., Sweetapple, M., Lindley, I.D., and Kirakar, J., 2013b, Hydrothermal Ni: Doriri Creek, Papua New Guinea: Ore Geology Reviews, v. 52, p. 37–57. DOI: 10.1016/j.oregeorev.2012.10.001.

Goodgame, V.R., 1997, The distribution and origin of arsenic and platinum group element mineralisation in the Mariners nickel deposit, Widgiemooltha, Western Australia: Unpublished Ph.D. thesis, University of Oregon, 115 p.

Gresham, J.J., and Loftus Hill, G.D., 1981, The geology of the Kambalda nickel field, Western Australia: Economic Geology, v. 76, p. 1373–1416.

Groves, D.I., Goldfarb, R.J., Robert, F., and Hart, C.J.R., 2003, Gold deposits in metamorphic belts: Overview of current understanding, outstanding problems, future research, and exploration significance: Economic Geology, v. 98, p. 1–29.

Hallberg, J.A., 1984, A geochemical aid to igneous rock type identification in deeply weathered terrain: Journal of Gochemical Exploration, v. 20, p. 1–8.

Hammond, R.L., and Nisbet, B.W., 1992, Toward a structural and tectonic framework for the Norseman-Wiluna Greenstone Belt, Western Australia, *in* Glover, J.E., and Ho, S.E., eds., The Archaean: Terrains, processes and metallogeny: University of Western Australia Geology Department, Publication 22, p. 39–50.

Hanley, J.J., and Bray, C.J., 2009, The trace metal content of amphibole as proximity indicator for Cu-Ni-PGE mineralization in the footwall of the Sudbury igneous complex, Ontario, Canada: Economic Geology, v. 104, p. 113–125.

Hanley, J.J., Pettke, T., Mungall, J.E., and Spooner, E.T.C., 2005, The solubility of platinum and gold in NaCl brines at 1.5 kbar, 600° to 800°C: A laser ablation ICP-MS pilot study of synthetic fluid inclusions: Geochimica et Cosmochimica Acta, v. 69, p. 2593–2611.

Hayward, N., 1988, Geology of the Widgiemooltha area and exploration progress to February 1988: WMC Resources Report, 144 p.

Heggie, G.J., Fiorentini, M.L., Barnes, S.J., and Barley, M.E., 2012, Maggie Hays Ni deposit: Part 2. Nickel mineralization and the spatial distribution of pge ore-forming signatures in the Maggie Hays Ni system, Lake Johnston greenstone belt, Western Australia: Economic Geology, v. 107, p. 817–833.

Hill, R.E.T., 1995, The volcanology of komatiites as deduced from field relationships in the Norseman-Wiluna greenstone belt, Western Australia: Lithos, v. 34, p. 159–188.

Keays, R.R., and Jowitt, S.M., 2013, The Avebury Ni deposit, Tasmania: A case study of an unconventional nickel deposit: Ore Geology Reviews, v. 52, p. 4–17. DOI: 10.1016/j.oregeorev.2012.07.001.

Ketris, M.P., and Yudovich, Y., 2009, Estimations of Clarkes for carbonaceous biolithes: World averages for trace element contents in black shales and coals: International Journal of Coal Geology, v. 78, p. 135–148.

Large, R.R., Bull, S.W., and Maslennikov, V.V., 2011, A carbonaceous sedimentary source-rock model for Carlin-type and orogenic gold deposits: Economic Geology, v. 106, p. 331–358.

Layton-Matthews, D., Lesher, C.M., Burnham, O.M., Liwanag, J., Halden, N.M., Hulbert, L., and Peck, D.C., 2007, Magmatic Ni-Cu-platinum-group element deposits of the Thomson Nickel Belt, *in* Goodfellow, W.D., ed., Mineral deposits of Canada: A synthethis of major deposit types, district metallogeny, the evolution of geological provinces, and exploration methods: Geological Association of Canada, Mineral Deposits Division, Special Publication no. 5, p. 409–432.

Lesher, C.M., 1989, Komatiite-associated nickel sulfide deposits, *in* Whitney, J.A., and Naldrett, A.J., eds., Ore deposition associated with magmas: Reviews in Economic Geology, v. 4, p. 45–100.

Lesher, C.M., and Groves, D.I., 1986, Controls on the formation of komatiite-associated nickel-copper sulfide deposits, *in* Friedrich, G., Genkin, A., Naldrett, A., Ridge, J., Sillitoe, R., and Vokes, F., eds., Geology and metallogeny of copper deposits: Springer Berlin Heidelberg, Society for Geology Applied to Mineral Deposits, Special Publication 4, p. 43–62.

Lesher, C.M., and Keays, R.R., 2002, Komatiite-associated Ni-Cu-(PGE) deposits: Mineralogy, geochemistry, and genesis, *in* Cabri, L.J., ed., The geology, geochemistry, mineralogy, and mineral benefication of the platinum-group elements: Canadian Institute of Mining, Metallurgy and Petroleum, v. 54, p. 579–617.

Lesher, C.M., Arndt, N.T., and Groves, D.I., 1984, Genesis of komatiite-associated nickel sulphide deposits at Kambalda, Western Australia: A distal volcanic model, *in* Buchanan, D.L., and Jones, M.J., eds., Sulphide deposits in mafic and ultramafic rocks: London, Institute of Mining and Metallurgy, p. 70–80.

Lesher, C.M., Burnham, O.M., and Keays, R.R., 2001, Trace-element geochemistry and petrogenesis of barren and ore-associated komatiites: The Canadian Minaralogist, v. 39, p. 673–696.

Le Vaillant, M., Barnes, S.J., Fisher, L., Fiorentini, M.L., and Caruso, S., 2014, Use and calibration of portable X-ray fluorescence analysers: Application to lithogeochemical exploration for komatiite-hosted nickel sulphide deposits: Geochemistry: Exploration, Environment, Analysis, DOI: 10.1144/geochem2012-166.

Lin, S., and Popp, R.K., 1984, Solubility and complexing of Ni in the system NiO-H_2O-HCl: Geochimica et Cosmochimica Acta, v. 48, p. 2713–2722.

Liu, W., Borg, S.J., Testemale, D., Etschmann, B., Hazemann, J.-L., and Brugger, J., 2011, Speciation and thermodynamic properties for cobalt chloride complexes in hydrothermal fluids at 35°-440°C and 600bar: An in situ XAS study: Geochimica et Cosmochimica Acta, v. 75, p. 1227–1248. DOI: 10.1016/j.gca.2010.12.002.

Liu, W., Migdisov, A., and Williams-Jones, A., 2012, The stability of aqueous nickel(II) chloride complexes in hydrothermal solutions: Results of UV-Visible spectroscopic experiments: Geochimica et Cosmochimica Acta, v. 94, p. 276–290. DOI: 10.1016/j.gca.2012.04.055.

Locmelis, M., Fiorentini, M.L., Barnes, S.J., and Pearson, N.J., 2013, Ruthenium variation in chromite from komatiites and komatiitic basalts: A potential mineralogical indicator for nickel sulfide mineralization: Economic Geology, v. 108, p. 355–364.

Marston, R.J., 1984, Nickel mineralisation in Western Australia: Geological Survey of Western Australia, Mineral Resources Bulletin 14, 271 p.

McCuaig, T.C., 1998, P-T-t-deformation-fluid characteristics of lode gold deposits: Evidence from alteration systematics: Ore Geology Reviews, v. 12, p. 381–453.

McCuaig, T.C., Beresford, S., and Hronsky, J., 2010, Translating the mineral systems approach into an effective exploration targeting system: Ore Geology Reviews, v. 38, p. 128–138. DOI: 10.1016/j.oregeorev.2010.05.008.

McKibben, M.A., Williams, A.E., and Hall, G.E.M., 1990, Solubility and transport of plantinum-group elements and Au in saline hydrothermal fluids: Constraints from geothermal brine data: Economic Geology, v. 85, p. 1926–1934.

McQueen, K.G., 1981, Volcanic-associated nickel deposits from around the Widgiemooltha dome, Western Australia: Economic Geology, v. 76, p. 1417–1443.

Pan, P., and Wood, S.A., 1994, Solubility of Pt and Pd sulfides and Au metal in aqueous bisulfide solutions: Mineralium Deposita, v. 29, p. 373–390.

Peters, W.S., 2006, Geophysical exploration for nickel sulfide mineralization in the Yilgarn Craton: Economic Geology, Special Publication 13, p. 167–193.

Pirajno, F., and González-Álvarez, I., 2013, A re-appraisal of the Epoch nickel sulphide deposit, Filabusi greenstone belt, Zimbabwe: A hydrothermal nickel mineral system?: Ore Geology Reviews, v. 52, p. 58–65. DOI: 10.1016/j.oregeorev.2012.11.005.

Platt, J.P., Allchurch, P.D., and Rutland, R.R., 1978, Archaean tectonics in the Agnew supracrustal belt, Western Australia: Precambrian Research, v. 7, p. 3–30.

Quinby-Hunt, M.S., Wide, P., and Berry, W.B.N., 1989, Element geochemistry of low-calcic black shales: Statistical comparison with other shales: U.S. Geological Survey circular 1037, v. 8–15.

Ryan, C.G., Kirkham, R., Hough, R.M., Moorhead, G., Siddons, D.P., de Jonge, M.D., Paterson, D.J., De Geronimo, G., Howard, D.L., and Cleverley, J.S., 2010, Elemental X-ray imaging using the Maia detector array: The benefits and challenges of large solid-angle: Nuclear Instruments and Methods in Physics Research Section A: Accelerators, Spectrometers, Detectors and Associated Equipment, v. 619, p. 37–43. DOI: 10.1016/j.nima.2009.11.035.

Said, N., Kerrich, R., Maier, W.D., and McCuaig, C., 2011, Behavior of Ni-PGE-Au-Cu in mafic-ultramafic volcanic suites of the 2.7 Ga Kambalda Sequence, Kalgoorlie terrane, Yilgarn craton: Geochimica et Cosmochimica Acta, v. 75, p. 2882–2910. DOI: 10.1016/j.gca.2011.02.032.

Sassani, D.C., and Shock, E.L., 1990, Speciation and solubility of palladium in aqueous magmatic-hydrothermal solutions: Geology, v. 18, p. 925–928.

——1998, Solubility and transport of platinum-group elements in supercritical fluids: Summary and estimates of thermodynamic properties for ruthenium, rhodium, palladium, and platinum solids, aqueous ions, and complexes to 1000°C and 5 kbar: Geochimica et Cosmochimica Acta, v. 62, p. 2643–2671.

Seat, Z., Stone, W.E., Mapleson, D.B., and Daddow, B.C., 2004, Tenor variation within komatiite-associated nickel sulphide deposits: Insights from the Wannaway deposit, Widgiemooltha dome, Western Australia: Mineralogy and Petrology, v. 82, p. 317–339. DOI: 10.1007/s00710-004-0047-3.

Seward, T.M., and Barnes, H.L., 1997, Metal transport by hydrothermal ore fluids, *in* Barnes, H.L., ed., Geochemistry of hydrothermal ore deposits: New York, John Wiley, p. 435–477.

Smith, B.H., 1984, Some observations on the geochemistry of gold mineralization in the weathered zone at Norseman, Western Australia: Journal of Geochemical Exploration, v. 22, p. 1–20.

Stone, W.E., and Archibald, N.J., 2004, Structural controls on nickel sulphide ore shoots in Archaean komatiite, Kambalda, Western Australia: The volcanic trough controversy revisited: Journal of Structural Geology, v. 26, p. 1173–1194. DOI: 10.1016/j.jsg.2003.11.014

Swager, C.P., 1997, Tectono-stratigraphy of the late Archaean greenstone terranes in the southern Eastern Goldfields, Western Australia: Precambrian Research, v. 83, p. 11–42.

Tagirov, B.R., and Baranova, N.N., 2009, The state of palladium in sulfide hydrothermal solutions: Experimental solubility study: Geochemistry International, v. 47, p. 1234–1242.

Tian, Y., Etschmann, B., Liu, W., Borg, S., Mei, Y., Testemale, D., O'Neill, B., Rae, N., Sherman, D. M., Ngothai, Y., Johannessen, B., Glover, C., and Brugger, J., 2012, Speciation of nickel (II) chloride complexes in hydrothermal fluids: In situ XAS study: Chemical Geology, v. 334, p. 345–363. DOI: 10.1016/j.chemgeo.2012.10.010.

Willett, G., Eshuys, E., and Guy, B., 1978, Ultramafic rocks of the Widgiemooltha-Norseman area, Western Australia: Petrological diversity, geochemistry and mineralisation: Precambrian Research, v. 6, p. 133–156.

Williams, P.R., and Whitaker, A.J., 1993, Gneiss domes and extensiomal deformation in the highly mineralised Archaean Eastern Goldfields Province, Western Australia: Ore Geology Reviews, v. 8, p. 141–162.

Wood, S.A., 2002, The aqueous geochemistry of the platinum-group elements with applications to ore deposits, *in* Cabri, L., ed., The geology, geochemistry, mineralogy and mineral beneficiation of platinum-group elements: Canadian Institute of Mining and Metallurgy, Special Publication 54, p. 211–249.

Wood, S.A., Mountain, B.W., and Fenlon, B.J., 1989, Thermodynamic constraints on the solubility of platinum and palladium in hydrothermal solutions: Reassessment of hydroxide, bisulfide, and ammonia complexing: Economic Geology, v. 84, p. 2020–2028.

Wood, S.A., Mountain, B.W., and Pan, P., 1992, The aqueous geochemistry of platinum, palladium and gold: recent experimental constraints and a re-evaluation of theoretical predictions: Canadian Mineralogist, v. 30, p. 955–982.

APPENDIX 1

Details of Analytical Method for Determination of Trace Elements In Situ by Laser Ablation ICP-MS Analyses on Gersdoffites from the Miitel Komatiite-Hosted Nickel Deposit

LA-ICP-MS

The LA-ICP-MS instrument used for this study consists of an Agilent 7700x ICP-MS coupled with a Resonetics RESolution M50-E, 193nm Excimer (5ns Pulse Width) laser recently equipped with the S155 Dual Volume Sample Cell. The laser lines (raster mode) were drilled across the mineral for 60s after measuring a gas blank for 2 0s. Ablation was carried out using a helium carrier gas and was mixed with argon before entering the ICP-MS. Compositions of various gersdorffite (NiAsS) grains in the following isotopes were determined: ^{34}S, ^{57}Fe, ^{59}Co, ^{61}Ni, ^{65}Cu, ^{66,68}Zn, ^{75}As, ^{82}Se, ^{95}Mo, ^{101}Ru, ^{103}Rh, ^{105,108}Pd, ^{109}Ag, ^{111}Cd, ^{118}Sn, ^{121}Sb, ^{128}Te, ^{185}Re, ^{189}Os, ^{193}Ir, ^{195}Pt, ^{197}Au, ^{208}Pb and ^{209}Bi.

Depending on the size of the mineral analyzed, the size of the laser beam varied from 15 μm to 44 μm, with a laser frequency of 15Hz, a power of 5mJ/pulse and a displacement speed of 5μm/s. Laser lines (raster mode) were drilled across minerals for 60s after measuring a gas blank for 20s. Each time beam sized was changed, a new batch of standards and monitors was analysed with the appropriate beam size.

All gersdorffite grains analyzed with LA-ICP-MS were analyzed by electron microprobe before, especially in order to know their composition in nickel, sulfur and iron. Electron microprobe analyses were carried out on the Cameca SX50 instrument at CSIRO in Perth. Microprobe data were collected by wavelength dispersive spectrometry at an accelerating voltage of 15Kv, beam current of 30nA and counting times of 60 seconds per element (30s peak 15s background on each side).

^{61}Ni was used as an internal standard to calculate the concentration of trace elements in the gersdorffite grains. The calibration and quality control were carried out by using Mass-3, Laflamme-Po727, Mass-1, UMSS1 and JBMSS5 reference materials. These reference materials have been used in previous studies (Barnes et al. 2008; Dare et al. 2010; Dare et al. 2011; Godel et al. 2012). A nickel blank was analyzed at the beginning and end of each analytical session to monitor and correct nickel interferences. Results obtained with the various monitors, analyzed as unknown samples for each run to check data quality, are shown in Table A1.

All the laser ablation ICP-MS data was reduced using Iolite software by subtracting gas background from each isotope analyzed. Sulfur, As, Ni, Si and Ca were monitored to ensure that the mineral measured were gersdorffite. The presence of accessory mineral Inclusions of accessory minerals within gersdorffite was monitored, and excluded from the time resolved spectrum before calculating the average signal; their signals were not taken into account during the integration leading to the calculation of trace elements concentrations in the mineral of interest. In order to monitor the quality of the data obtained with ^{61}Ni as internal standard and MASS3 as calibrant, the results were compared with results obtained with ^{34}S as internal standard and Laflamme (Po727) as calibrant. Results are shown for ^{101}Ru, ^{103}Rh, ^{105,108}Pd, ^{189}Os, ^{193}Ir, ^{195}Pt and ^{197}Au in Fig. A1. Finally, Table A2 lists the detection limits obtained for the main elements of interests in function of the beam size used.

LA-ICP-MS interference

There is a possible interference on determining ^{101}Ru in nickel arsenide which must be evaluated. This interference is caused by argide (^{40}Ar) interference with ^{61}Ni on ^{101}Ru. In order to correct for this interference, a nickel blank was analyzed at each run. Using the results obtained for ^{101}Ru with this nickel blank, we could account for the amount of ^{101}Ru produced for 1% of Ni present in the mineral phase analyzed. All the results obtained were then corrected before calculation of trace elements concentrations.

TABLE A1. Analyses of Reference Materials Used in the Calibration of LA-ICP-MS and In-House Reference Materials Used to Monitor the Data Quality

Element		^{107}Ag	^{75}As	^{197}Au	^{209}Bi	^{111}Cd	^{59}Co	^{65}Cu	^{57}Fe	^{193}Ir	^{189}Os	^{208}Pb	^{105}Pd	^{195}Pt	^{103}Rh	^{101}Ru	^{33}S	^{121}Sb	^{118}Sn
		ppm	ppm	ppm	ppm	ppm	ppm	ppm	%	ppm	ppm	ppm	ppm	ppm	ppm	ppm	%	ppm	ppm
D.L		0.01	2	0.002	0.003	0.03	0.08	0.002	n.d.	0.002	0.009	0.008	0.019	0.006	0.005	0.024	n.d.	0.01	0.03
Reference materials used for calibration																			
		MASS –3	MASS –3	MASS –3	MASS –3	MASS –3	MASS –3	MASS –3	MASS –3	MASS –3	MASS –3	MASS –3	MASS –3	MASS –3	MASS –3	MASS –3	MASS –3	MASS –3	MASS –3
Working value		69.9	68.8	53.8	64.8	99.6	75.5	77.9	0.1	62.5	73.6	79.7	58.0	33.8	20.9	67.3	21.96	48.3	52.6
	Stdev	11.9	7.3	10.6	12.5	17.4	10.7	12.5			5.5	13.7			2.8		4.8	6.5	18.3
	Determined by	avg/ mass1/ gse/jb	avg/ mass1/ gse/jb	avg/po/ mass1/ gse/jb	avg/ mass1/ gse/jb	avg/ mass1/ gse	avg/ mass1/ gse	avg/ mass1/ gse/jb		ID	avg'po 727+JB	avg/ mass1/ gse/jb	ID	ID	avg po/ jb5	ID	probe	avg/ mass1/ jb	avg/ mass1/ gse
Values obtained for in-house reference materials																			
JBMSS5: FeS doped for PGE, Ag, As, Au, Bi, Cu, Pb, Ni, Re, Sb, Se, Te																			
Working value		60.7	79.0	35.9	76.1	0.13	0.28	0.021	57.0	44.0	42.6	71.5	64.1	47.0	61.4	21.7	40.0	61.3	0.34
Fe-IS	Stdev	3.7	11.0	4.8	2.9	0.04	0.02	0.001	0.90	n.d.	0.93	4.5	n.d.	n.d.	7.2	n.d.	0.60	7.3	0.03
	Determined by	ICP-sol	ICP-sol	ICP-sol	ICP-sol	NIST 610	NIST 610	Cu-blk	Po-727	ID-sol at UQAC	ICP-sol	ICP-sol	ID-sol at UQAC	ID-sol at UQAC	ICP-sol	ID-sol at UQAC	Po-727	ICP-sol	NIST 610
This study	Average	47.1	67.8	24.7	63.6	0.1	0.3	155.0	51.08	38.6	46.1	60.7	47.1	35.2	48.9	17.0	32.5	37.6	0.1
n = 10	Stdev	1.9	19.1	1.4	3.3	0.30	0.2	6.5	5.47	1.5	2.0	2.1	1.9	1.6	1.3	0.9	0.9	1.9	0.1
UQAC-MSS1: $NiFeS_2$ doped for PGE, Au																			
Working value		0.27	1.9	1.21	<0.02	0.27	98.5	0.003	30.3	1.37	1.90	2.2	1.26	1.66	0.94	1.75	38.0	0.08	2.9
Fe-IS	Stdev	0.08	0.21	0.24	100	0.06	1.2	0.001	1.3	0.01	0.01	0.54	0.05	0.01	0.01	0.03	0.50	0.03	0.57
	Determined by	NIST 610	NIST 610	NIST 610	NIST 610	NIST 610	NIST 610	NIST 610	EMP	ID-sol at Leoben	ID-sol at Leoben	NIST 610	ID-sol at Leoben	ID-sol at Leoben	Po-727	ID-sol at Leoben	EMP	NIST 610	NIST 610
This study	Average	0.11	23.2	0.73	0.02	0.15	74	15.080	26.93	1.23	1.10	1.2	1.05	1.33	0.75	1.78	31.0	0.09	1.4
n = 10	Stdev	0.05	18.55	0.23	0.01	0.37	1.3	2.880	2.21	0.13	0.12	0.44	0.20	0.23	0.06	0.39	1.71	0.07	0.41

Notes: Detection limit = 3 x (BC)1/2 x C/I, where BC is background counts, C is concentration of analyte in the reference material, and I is peak intensity of the analyte; Int Std = Internal standard; Wilson 02 published values from Wilson et al., 2002; UQMSS1 UQAC-MSS1 in-house reference material; EMP = electron microprobe at McGill University; ID-sol = solution by isotopic dilution followed by ICP-MS, NIST610 LA-ICP-MS using NIST-610 glass and Cu as the internal standard except Ni in the case of UQAC-MSS1 to calibrate at UQAC; SQ = semiquantification option of Plasma Lab using NIST610 to calibrate at UQAC; ICP-sol = solution by aqua regia followed by ICP-MS at UQAC; AA = solution by aqua regia followed by atomic absorption at UQAC, Cu-blk LA-ICP-MS using Cu blank bead to calibrate at UQAC, Stdev = standard deviation, n = number of analyses, n.d. = not determined

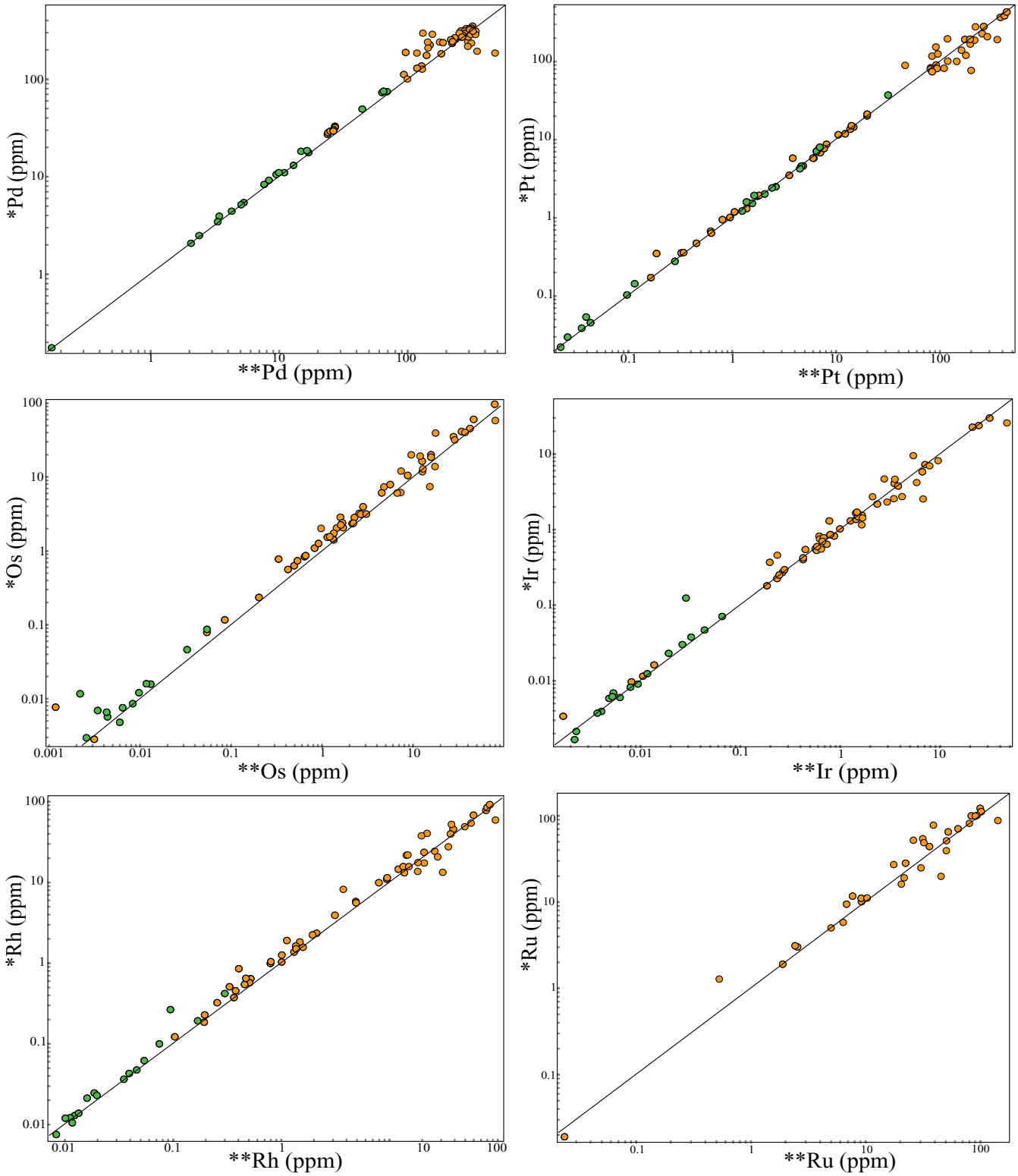

FIG. A1. Comparison of results obtained for trace element concentration calculation using LA-ICP-MS results with two different methodologies: (*) Using S as internal standard and LAF (Po727) as calibrant, and (**) using Ni as internal standard and MASS-3 as calibrant.

TABLE A2. Detection Limits are Calculated for Integrations Using MASS 3 as Calibrant and 62Ni as Internal Standard and MASS 3 as Calibrant

Beam size		^{107}Ag	^{197}Au	^{193}Ir	^{189}Os	^{105}Pd	^{195}Pt	^{103}Rh	^{101}Ru	^{121}Sb	^{82}Se	^{118}Sn
44	AV	0.0024	0.0004	0.0006	0.0011	0.0070	0.0010	0.0011	0.0060	0.0020	0.0746	0.0019
	MD	0.0020	0.0003	0.0005	0.0009	0.0062	0.0009	0.0009	0.0051	0.0017	0.0653	0.0016
	SD	0.0014	0.0002	0.0003	0.0005	0.0041	0.0005	0.0006	0.0034	0.0011	0.0371	0.0010
	ASD	56.6280	56.8850	49.3647	50.2109	58.7904	50.1000	53.0788	56.7988	57.2632	49.7036	54.1138
33	AV	0.0030	0.0004	0.0007	0.0016	0.0082	0.0012	0.0015	0.0074	0.0025	0.0853	0.0026
	MD	0.0026	0.0004	0.0007	0.0012	0.0074	0.0011	0.0012	0.0065	0.0021	0.0718	0.0023
	SD	0.0015	0.0002	0.0004	0.0009	0.0042	0.0007	0.0010	0.0036	0.0015	0.0413	0.0014
	ASD	49.1386	47.1481	55.7860	58.6343	50.8973	56.1583	67.7288	47.9180	59.3601	48.4514	53.8457
26	AV	0.0034	0.0006	0.0009	0.0018	0.0109	0.0017	0.0016	0.0091	0.0031	0.0993	0.0030
	MD	0.0030	0.0006	0.0008	0.0017	0.0094	0.0017	0.0014	0.0076	0.0026	0.0891	0.0027
	SD	0.0017	0.0003	0.0005	0.0006	0.0057	0.0008	0.0007	0.0042	0.0014	0.0481	0.0013
	ASD	48.7897	44.8496	51.6412	33.0422	52.6558	46.9927	45.5829	45.8110	44.0553	48.4766	44.5627
15	AV	0.0149	0.0037	0.0038	0.0100	0.0420	0.0092	0.0065	0.0400	0.0140	0.7490	0.0130
	MD	0.0084	0.0021	0.0023	0.0053	0.0269	0.0046	0.0035	0.0217	0.0081	0.3832	0.0080
	SD	0.0203	0.0051	0.0043	0.0159	0.0554	0.0117	0.0090	0.0555	0.0205	1.6104	0.0168
	ASD	136.5326	136.2719	113.7737	159.7426	132.0078	127.2672	137.3877	138.6835	146.1140	215.0016	128.8125

AV = average, MD = median, SD = standard deviation on n analyses, ASD = absolute standard deviation = (SD/AV)*100